An updated fast continuous contact detection algorithm and its implementation in case study of ice-structure interaction by Peridynamics

Yuan Zhang, Longbin Tao, Liyu Ye*, Chao Wang, Shuai Sun, Wenjun Lu

[a] College of Shipbuilding Engineering, Harbin Engineering University, Harbin 150001, China

[b] Norwegian University of Science and Technology (NTNU), Trondheim, Norway

[c] School of Naval Architecture and Ocean Engineering, Jiangsu University of Science and Technology, Zhenjiang 212003, China

[d] Department of Naval Architecture and Marine Engineering, University of Strathclyde, Glasgow G4 0LZ, United Kingdom

[e] Qingdao Innovation and Development Base of Harbin Engineering University, Qingdao 266400, China

[f] National Key Laboratory of Transient Physics, Nanjing University of Science and Technology, Nanjing 210094, China

ABSTRACT

Peridynamics is a mesh-free particle method that has been proposed in the last two decades. Contact between bodies in Peridynamics is a challenging and critical phenomenon that not only affects the computational efficiency of the algorithm, but is also closely related to the accuracy of the calculations. Therefore, it is important to develop a contact detection algorithm that is efficient, accurate, easy to extend to coupled numerical methods, and conducive to parallel computation. This study proposes a fast and continuous contact detection algorithm (FCCDA) that consists of two main parts. The first involves establishing a regular box bounding the entire target of collision to avoid the unnecessary calculation of material points that are not in contact with it, where this critically reduces the number of time-consuming calculations. The second part is a graphics-based algorithm to identify specific particles that penetrate the target. Both the numerical strategies and the mathematical methodologies of the FCCDA are discussed here. It was embedded into a Peridynamics system and

* Corresponding author.

E-mail address: yeliyuxrxy@hrbeu.edu.cn.

This is a peer-reviewed, accepted author manuscript of the following research article:
Zhang, Y., Tao, L., Ye, L., Wang, C., Sun, S., & Lu, W. (2023). An updated fast continuous contact detection algorithm and its implementation in case study of ice-structure interaction by peridynamics. Marine Structures, 89, [103406]. https://doi.org/10.1016/j.marstruc.2023.103406

examined in the context of a benchmark case for verification. Ship–ice interaction and propeller–ice interaction are also demonstrated using the proposed algorithm as examples of its applications to engineering.

Keywords: Fast continuous contact detection algorithm (FCCDA), Peridynamics, ice-ship interaction, ice-propeller interaction

1. Introduction

Compared with mesh-based algorithms, mesh-free material particle methods (MPM) such as Peridynamics (PD) and smooth particle hydrodynamics (SPH), do not require the remeshing process, and are thus better suited for simulating problems involving large deformations, for example, bending failure, crack propagation, and other discontinuities. The MPM has had a significant impact on computational mechanics, and has been applied to a variety of engineering problems [1-3]. The detection of contact in case of impact between objects in the MPM is a critical and challenging issue.

PD, a representative MPM, has been developed in a variety of fields in solid mechanics. The governing equation of the PD is in integral form rather than differential form. Therefore, it has the advantage to solve the problems of large deformation and fracture. In addition to the deformation of and damage to objects under simple boundary conditions, most engineering problems involve interactions between structures, and PD is a useful tool to study and predict impact-based fracture [4, 5]. A contact model is needed to identify the impact between bodies. In most cases of contact, both bodies are discretized according to whether the impactor is rigid or deformable. An example is the contact between different materials and structures [6-8]. The advantages of this kind of mesh-free discretization in the contact model are as follows:

1) The collision between bodies with complex shapes can be easily modeled by using discrete particles.

2) Identifying contact is easy to achieve since the contact detection equals to judgement of relative position between points in space.

3) All objects in contact are discretized by the equation of the particle method.

However, this method cannot be applied to impactors in mesh discretization. Moreover, a heavy computational burden is incurred when the impactor is rigid because searching for particles is time consuming in the MPM, and takes up to 60%–80% of the total time [9]. We thus recommend this kind of contact model only in the case all bodies in contact are governed by the MPM equation. A contact model based on a simply shaped impactor has also been introduced [10, 11]. The impactor in this case is a rigid body with a regular shape, such as a cylinder or a sphere. Contact is identified easily by calculating the distance between the particles and the centroid of the impactor. This method guarantees computational efficiency because the unnecessary particle search operation is no longer required, such as in case of contact between the PD domain and a regular-shaped structure [12, 13], and most damage modeling reviewed by Mewael et al. [4]. However, the shape of the impactor used in engineering is not regular, because of which it is difficult to find the centroid or a specific law to determine whether the particle penetrates the object of collision. A point-to-plane distance algorithm has been introduced for the convex polyhedron by Vazic [14].

This study develops an efficient and accurate contact detection algorithm for PD that is easily applicable to engineering analysis. The remainder of this paper is organized as follows: A brief overview of PD theory is introduced in Section 2, which helps illustrate the implementation of fast and continuous contact detection algorithm (FCCDA) to the PD framework. In Section 3, we detail

the method and mathematical principle of the graphics-based fast and continuous contact detection algorithm (FCCDA). The numerical implementation of the proposed algorithm is analyzed in Section 4. To validate it, benchmark cases were examined by embedding it into Peridynamics (PD), and the results are compared with those of the Finite Element Method (FEM) in Section 5. The application of the proposed method to engineering is demonstrated in Section 6.

2. Peridynamics theory

This section briefly introduces the theory of Peridynamics (PD). The governing equations, their numerical discretization, and a contact model are provided.

2.1 Fundamentals of PD

PD is a non-local method that uses integral operators, instead of the spatial derivatives used in traditional solid mechanics, to describe discontinuities and large deformations within a continuous body. The domain is discretized by particles that interact only with their neighbors at a certain distance, usually known as the horizon (H_x). Figure 1 shows the principle of PD theory: Particle i at location $\mathbf{x}$ interacts with particle j located in $\mathbf{x}'$. They have displacements $\mathbf{u}$ and $\mathbf{u}'$, respectively, when the body is deformed by an external force. The deformation results in a force density $\mathbf{t}$ of i acting on j, and $\mathbf{t}'$ of j acting on i. Then, the equation of motion of a material point in PD theory is given by Madenci and Oterkus [11] as:

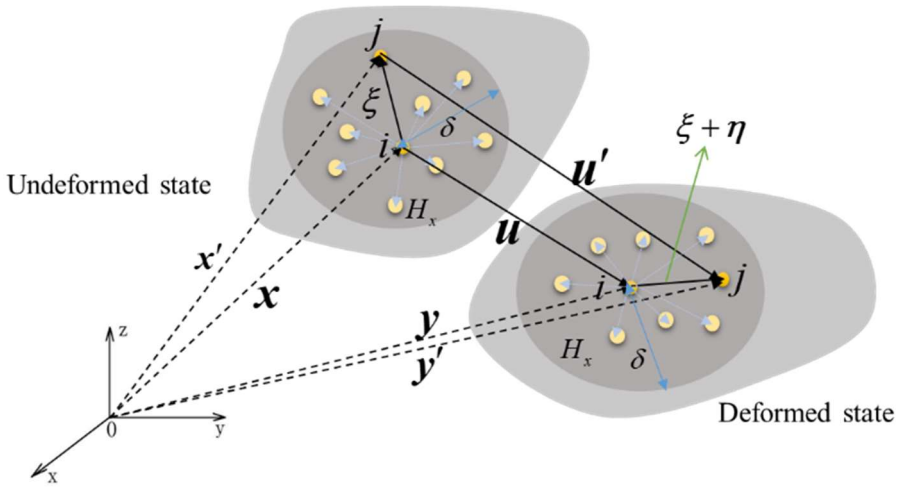

FIGURE 1 Schematic diagram of particle interactions in PD theory [15]

$$\rho(\mathbf{x})\ddot{\mathbf{u}}(\mathbf{x},t) = \int_{H_x} (\mathbf{t}(\mathbf{u}'-\mathbf{u},\mathbf{x}'-\mathbf{x},t) - \mathbf{t}'(\mathbf{u}-\mathbf{u}',\mathbf{x}-\mathbf{x}',t))dV' + \mathbf{b}(\mathbf{x},t)\,, \tag{1}$$

where $\rho(\mathbf{x})$ is the density of the material and $\ddot{\mathbf{u}}(\mathbf{x},t)$ is the acceleration of the particle. According to the state of the pairwise force density, PD is defined in three forms:

1) Bond-based PD (BB-PD): This is a special case that assumes that the vectors $\mathbf{t}$ and $\mathbf{t}'$ of force density are equal in magnitude, and are parallel to the relative position vector. Under this assumption, Poisson's ratio is fixed at 1/3 in 2D and ½ in 3D. The force density in Equation (1) is:

$$\mathbf{t} = -\mathbf{t}' = 2\delta sb\frac{\mathbf{y}'-\mathbf{y}}{|\mathbf{y}'-\mathbf{y}|}. \tag{2}$$

2) Ordinary state-based PD (OSB-PD): The magnitudes of the vectors of force density are not equal to each other compared with the BB-PD. Then, the Poisson ratio has no limitation, and the force density is given as:

$$\begin{cases} \mathbf{t} = \dfrac{1}{2}\left\{\dfrac{4\delta d\Lambda a\theta}{|\mathbf{x}'-\mathbf{x}|} + 4\delta sb\right\}\dfrac{\mathbf{y}'-\mathbf{y}}{|\mathbf{y}'-\mathbf{y}|} \\ \mathbf{t}' = -\dfrac{1}{2}\left\{\dfrac{4\delta d\Lambda a\theta'}{|\mathbf{x}-\mathbf{x}'|} + 4\delta sb\right\}\dfrac{\mathbf{y}'-\mathbf{y}}{|\mathbf{y}'-\mathbf{y}|} \end{cases}. \tag{3}$$

3) Non-ordinary state-based PD (NOSB-PD): The force density has no limitation in terms of direction, and there is no restriction on the material properties in NOSB-PD. The following relationship must hold [16]:

$$\int_{H_x} \left\{(\mathbf{y}'-\mathbf{y})\times\mathbf{t}(\mathbf{x},t)\langle\mathbf{x}'-\mathbf{x}\rangle\right\}dV' = 0\,, \tag{4}$$

in which

$$\mathbf{t}(\mathbf{x},t)\langle\mathbf{x}'-\mathbf{x}\rangle = w\langle\mathbf{x}'-\mathbf{x}\rangle\mathbf{P}\mathbf{K}^{-1}(\mathbf{x}'-\mathbf{x})\,. \tag{5}$$

Note that in the above formula, a, b, and d are the parameters of PD, δ represents the size of the horizon, Λ is an auxiliary parameter of PD, θ and θ' are the dilatations of particles i and j, respectively, s is the stretch between particles, and is the key variable of the failure criterion, $\mathbf{P}$ is the first-order Piola–Kirchhoff (Lagrangian) stress tensor, and $\mathbf{K}$ is the explicit form of the shape tensor. Details of $\mathbf{P}$ and $\mathbf{K}$ are provided in Ref. [11].

The OSB-PD is the representative form for illustrating the coupling of the FCCDA and PD because it has no restriction on the Poisson ratio, ensures stable computing, and is the most widely used of the three forms in engineering [15, 17-21].

2.2 Contact modeling in PD

The model of impact with a rigid target in the PD domain was first proposed by Silling in EMU

code [22], and was then presented in detail in Ref. [11]. At time t, the impactor located in $\mathbf{x}_{(pen)}^{t}$ and the PD domain move with velocities, $\mathbf{v}_{(pen)}^{t}$ and $\mathbf{v}_{(i)}^{t}$, respectively. The position and the displacement of particle i are $\mathbf{x}_{(i)}^{t}$ and $\mathbf{u}_{(i)}^{t}$, respectively, as shown in Figure 2(a). As the objects move to their new locations, $\mathbf{x}_{(pen)}^{t+\Delta t}$ and $\mathbf{x}_{(i)}^{t+\Delta t}$, contact occurs at time $t+\Delta t$, and results in the particles penetrating the impactor. Their vector of relative position is $\mathbf{x}_{(rel)}^{t+\Delta t}$, as shown in Figure 2(b). However, such penetration does not occur in fact. The penetrated particle thus needs to be relocated to its new position $\overline{\mathbf{x}}_{(i)}^{t+\Delta t}$ outside the impactor, as shown in Figure 2(c). The allocation of new positions refers to the principle of the nearest distance.

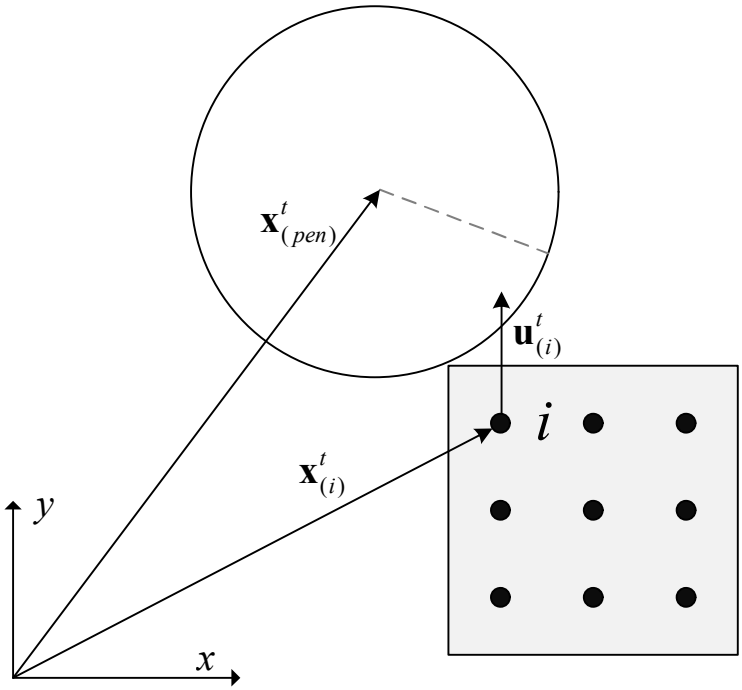

(a) Time, t

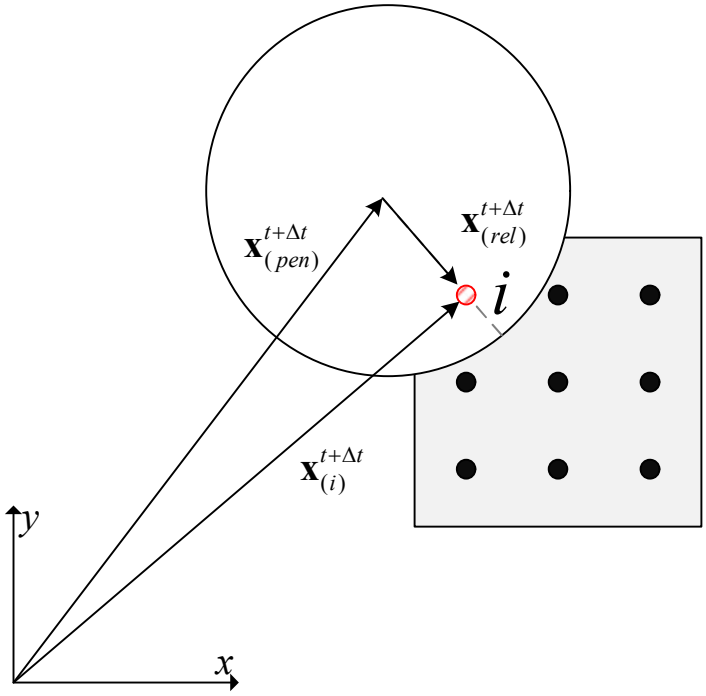

(b) Time, $t+\Delta t$

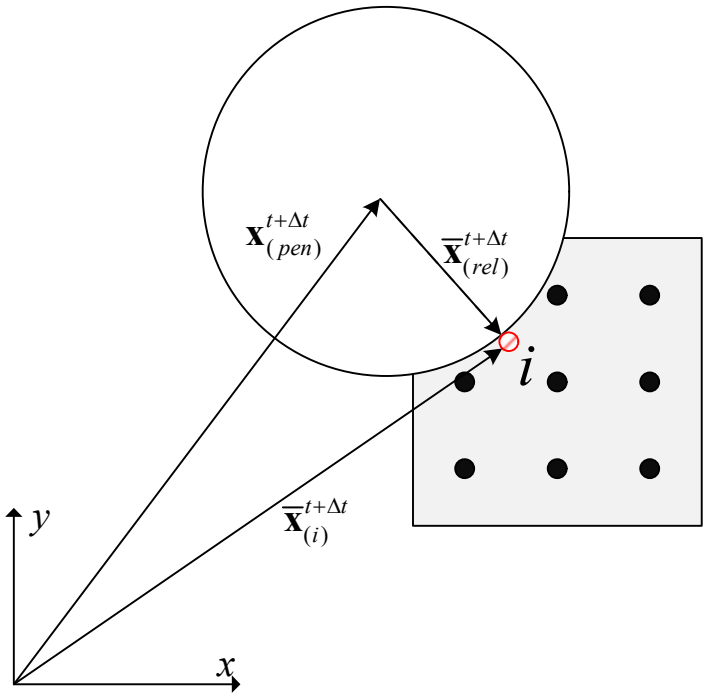

(c) Time, $t+\Delta t$

FIGURE 2 Contact modeling in PD theory.

The contact process described above involves two stages: One involves detecting the penetrating particles, and the other involves reassigning their positions and calculating the contact force. Contact is identified by calculating the distance between the particle and the centroid of the impactor. The location of particle i at time $t+\Delta t$ is:

$$\mathbf{x}_{(i)}^{t+\Delta t}=\mathbf{x}_{(i)}^{t}+\mathbf{u}_{(i)}^{t}. \tag{6}$$

Then, the criterion used to judge whether the particles penetrate the impactor is:

$$\lambda_{(i)}^{t+\Delta t}=\begin{cases}1 & \text{if } \mathbf{x}_{(rel)}^{t+\Delta t}=\mathbf{x}_{(i)}^{t+\Delta t}-\mathbf{x}_{(pen)}^{t+\Delta t}\le r,\text{contact}\\ 0 & \text{if } \mathbf{x}_{(rel)}^{t+\Delta t}=\mathbf{x}_{(i)}^{t+\Delta t}-\mathbf{x}_{(pen)}^{t+\Delta t}> r,\text{noncontact}\end{cases}, \tag{7}$$

where r represents the radius of the impactor. Contact detection is thus completed.

The next stage involves redistributing the penetrated particles according to the closest distance principle. A particle is relocated to $\overline{\mathbf{x}}_{(i)}^{t+\Delta t}=\mathbf{x}_{(pen)}^{t+\Delta t}+\overline{\mathbf{x}}_{(rel)}^{t+\Delta t}$, where $\overline{\mathbf{x}}_{(rel)}^{t+\Delta t}$ is collinear and has the same direction as $\mathbf{x}_{(rel)}^{t+\Delta t}$. The velocity of the particle in its new location is:

$$\overline{\mathbf{v}}_{(i)}^{t+\Delta t}=\frac{\dot{\overline{\mathbf{x}}}_{(i)}^{t+\Delta t}-\dot{\mathbf{x}}_{(i)}^{t}}{\Delta t}. \tag{8}$$

The contact force resulting from the particle in contact and the total force are:

$$\mathbf{F}_{(i)}^{t+\Delta t}=-1\times\rho_{(i)}\frac{\overline{\mathbf{v}}_{(i)}^{t+\Delta t}-\mathbf{v}_{(i)}^{t+\Delta t}}{\Delta t}V_{(i)}, \tag{9}$$

and

$$\mathbf{F}^{t+\Delta t}=\sum_{i=1}\mathbf{F}_{(i)}^{t+\Delta t}\lambda_{(i)}^{t+\Delta t}. \tag{10}$$

3. Fast and continuous contact detection algorithm (FCCDA)

The method of contact detection described in Section 2.2 is limited to regular-shaped impactors. It is difficult to determine whether the particle comes into contact with impactor owing to its irregular shape in most impact events in practice. The proposed FCCDA is decomposed into two main steps:

the bounding box presented in Section 3.1, and the contact detection algorithm presented in Section 3.2. The algorithm also involves calculating the contact normal presented in Section 3.2. Furthermore, the proposed algorithm is easily to achieve the parallel computing which is present in our other work [15].

3.1 Establishing the bounding box

The idea of the bounding box was originally presented for the finite element method (FEM) [23, 24] as shown in Figure 3(a). The bounding box was established to surround the face of the element in both its known location and its predicted position. To find FEM nodes in contact, the dimensions of the bounding box are determined by the maximum distance that a node in contact can move. The point-in-box search algorithm is used to detect element nodes inside the bounding box. The bounding box was subsequently extended to the discrete element method (DEM), to which its improved model was widely applied [25, 26] as shown in Figure 3(b). The bounding box method requires identifying all cells that may be occupied by any part of the target particles, listing the target particles in these cells, and searching for potential contact in the same group of cells (“bounding box”). The bounding box model proposed here uses the same main idea and has the purpose as the model above. However, it is specially designed for the mesh-free particle method of the same type of PD method.

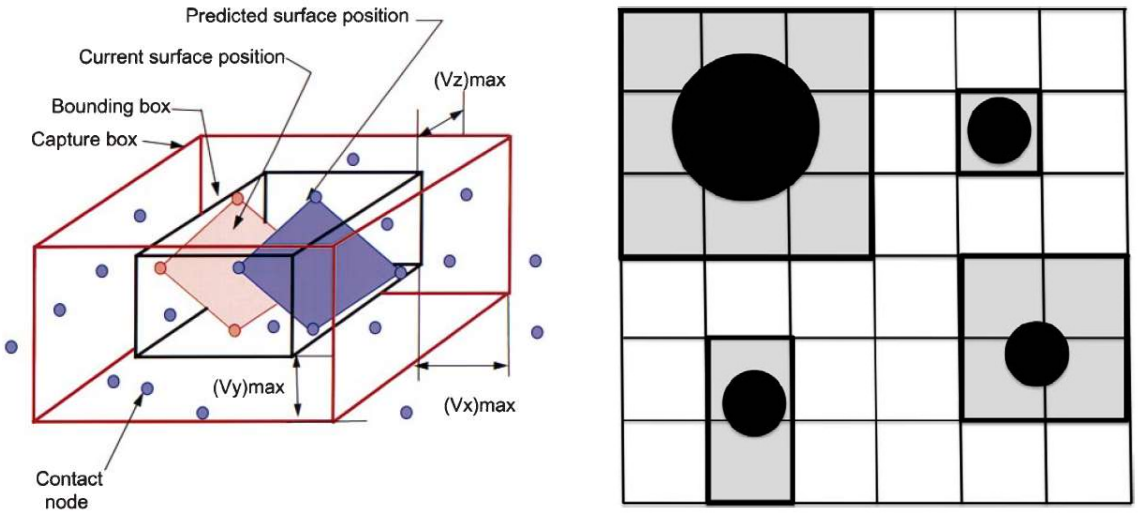

(a) The bounding box in FEM [27]

(b) The bounding box in DEM [26]

FIGURE 3 The diagrammatic sketch of the bounding box in the FEM and DEM.

The most time-consuming calculation in PD involves particle search in horizon definition and time integration [11]. The contact detection is implemented in the process of force integration of each particle at each time step. To reduce the computational cost caused by the unnecessary search of material points that never contact at each time step, the bounding box is developed before contact detection to include all the potential particles that may contact the impactor at the current time step. It begins by establishing a regular-shaped space box containing the impactor at all times. The box moves with the impactor and their (box and impactor) relative positions remain unchanged. Thus, the shape of the bounding box is changeable; it can be a circle, cube, or polyhedron depending on the shape of the impactor. The design principles of the bounding box are as follows: 1) It has a regular and simple shape (hexahedron is the best choice) such that it is easy to directly judge whether a given point is inside the box. 2) The box is a polyhedron with the smallest surface area and the lowest volume needed to surround the entire impactor.

Below are three examples illustrating how the bounding box is designed and works.

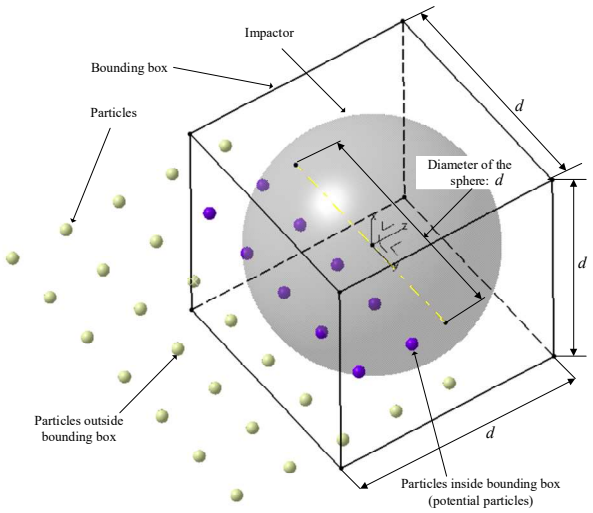

FIGURE 4 Hexahedral bounding box in example 1.

Example 1. The particle domain impacts the sphere. A hexahedral bounding box is established containing the impact. Only particles inside the hexahedron are potential points in contact with the surface of the impactor, as shown in Figure 4. The hexahedral bounding box is the most common one used in impact problems, and the impactor in Figure 4 can have any shape, such as a cylinder, irregular bottle, hull, and an automobile.

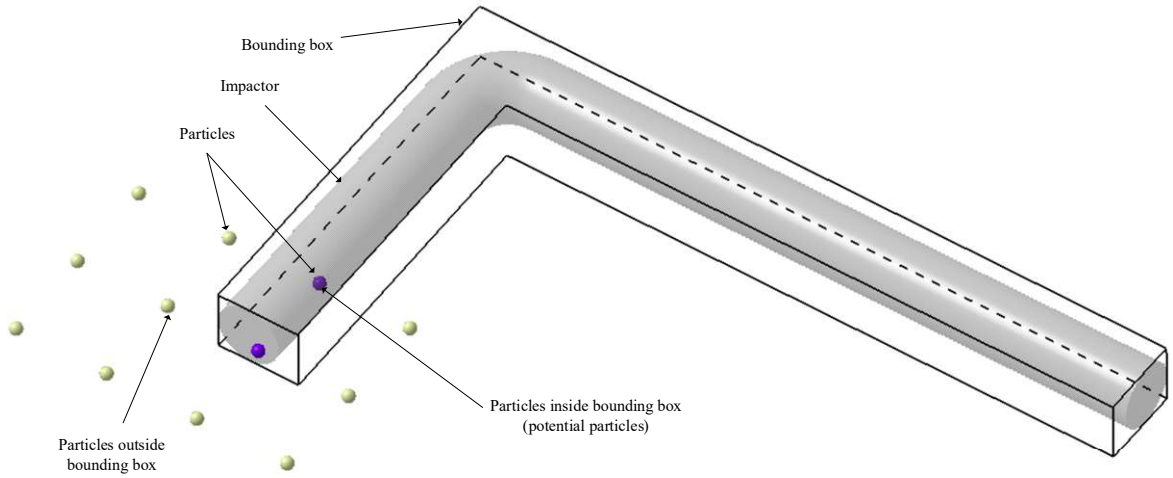

FIGURE 5 The combined shape of a bounding box of multiple hexahedrons in example 2

Example 2. Although the hexahedron can be used as a bounding box, there is still extra space not occupied by the collision body, as shown in Figure 5. Therefore, the combined shape of multiple hexahedrons is used as the optimal bounding box.

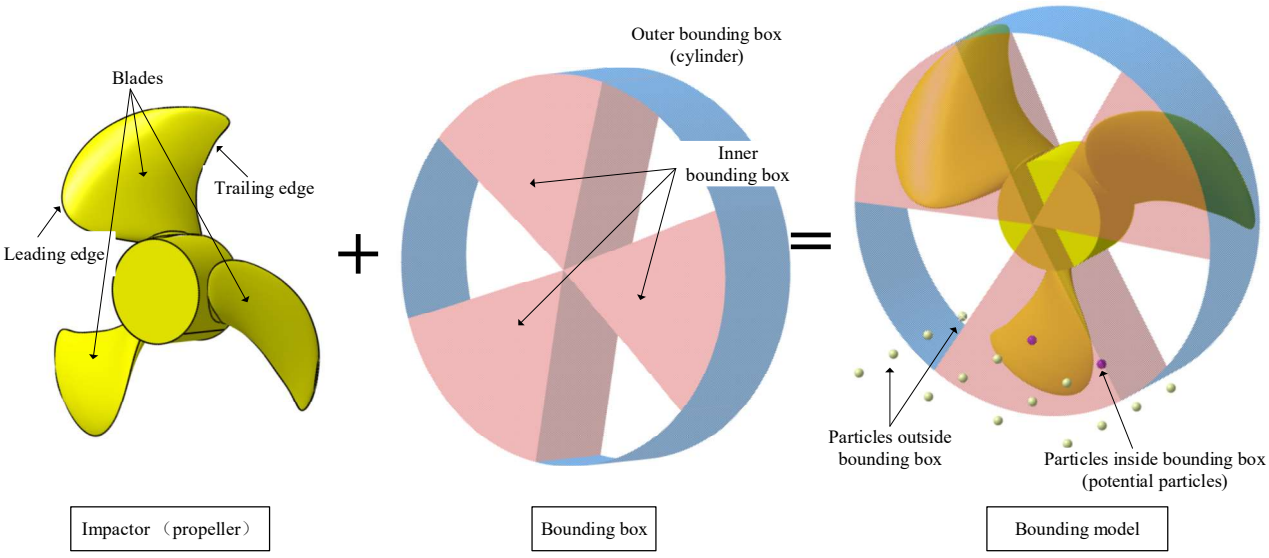

FIGURE 6 Bounding box in example 3

Example 3. Some objects with very complex shapes cannot be surrounded by simple hexahedrons, and collision between complex targets and the particle domain is accompanied by complex contact-related issues caused by their motion. In this case, the method of modeling the bounding box must be analyzed according to the given situation. For example, as shown in Figure 6, the propeller is an impactor that rotates over time. Two boxes are combined to bound it: a cylinder surrounding the entire propulsion system; and a fan-shaped space that contains blades, and moves with them. Consequently, the bounding algorithm is divided into two steps as follows:

1) If the particles are inside the cylinder, then go to (2);
2) If the particles are inside the fan space, then go to the procedure for contact detection in Section 2.2.

3.2 Contact detection algorithm

This section proposes the algorithm for determining the specific particles in contact and calculating their motion-related information.

The colliding object is discretized into a sufficient number of quadrilateral/triangular panel elements to express its shape, where this is similar to the mesh discretization method in the FEM. Each panel element is treated as a spatial plane; then, contact detection is simplified as a problem of analytic geometry, one of determining the relative position between points and planes. The contact detection process involves the following steps:

1) Preprocessing. The impactor is discretized by using a commercial software or a meshing program. However, the node labels of all planar elements should be uniformly arranged in clockwise or counterclockwise order, which facilitates the determination of the directions of their normal vectors. Examples are illustrated in Figure 7: A sphere is discretized into triangle elements represented in grid format by three nodes numbered in counterclockwise order, and a cylinder is discretized into quadrilateral elements represented in grid format by four nodes numbered in counterclockwise order.

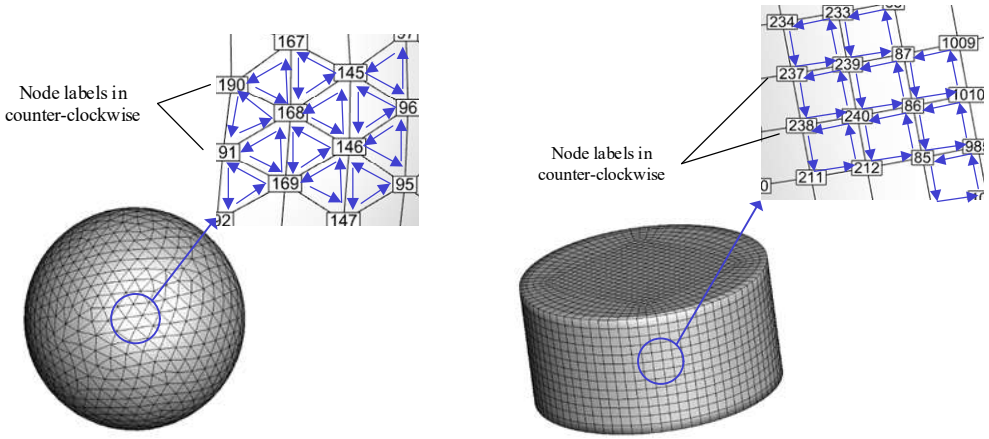

FIGURE 7 Examples of discretization of the impactor

2) Search for planar elements that may come into contact with the particles. Several variables need to be declared, and all position vectors of particles inside the bounding box, $\mathbf{x}_{(p)}$, are

stored in an infinite-dimensional array or a vector state $\underline{\mathbf{X}}$ (a concept defined in PD theory [11]):

$$\underline{\mathbf{X}}(\mathbf{x}_{(p)},t)=\begin{Bmatrix}\mathbf{x}_{(p1)}\\ \vdots \\ \mathbf{x}_{(p\infty)}\end{Bmatrix}=\begin{Bmatrix}(x_{p1},y_{p1},z_{p1})\\ \vdots \\ (x_{p\infty},y_{p\infty},z_{p\infty})\end{Bmatrix}. \tag{11}$$

All nodes of the discretized impactor are stored in $\underline{\mathbf{IM}}$:

$$\underline{\mathbf{IM}}(\mathbf{m}_{(n)},t)=\begin{Bmatrix}\mathbf{m}_{(n1)}\\ \vdots \\ \mathbf{m}_{(n\infty)}\end{Bmatrix}=\begin{Bmatrix}(x_{n1},y_{n1},z_{n1})\\ \vdots \\ (x_{n\infty},y_{n\infty},z_{n\infty})\end{Bmatrix}. \tag{12}$$

Each planar element of the discretized impactor is dominated by its node, and a state of node numbers is defined here as $\underline{e}$:

$$\underline{e}=\begin{Bmatrix}e_{(1)}\\ e_{(2)}\\ \vdots \\ e_{(\infty)}\end{Bmatrix}=\begin{Bmatrix}n_j,n_k,n_q,n_r\\ n_l,n_g,n_k,n_j\\ \vdots \\ \vdots \end{Bmatrix}, \tag{13}$$

where n_j, n_k, n_q, and n_r are all positive integer scalars representing the number of vectors in the state $\underline{\mathbf{IM}}$, and their order follows the rules in the previous step. For example, n_j is the number of the first control nodes of the first element $e_{(1)}$.

A computational geometry-based criterion is introduced to identify the planar elements with which the particle might collide. If a material point is located in the hexahedron space occupied by the impactor element at time step t, it is assumed that these two may come into contact. As shown in Figure 8, two planar quadrilateral elements $e_{(1)}$ and $e_{(2)}$ are defined by four nodes each, $\{n_j,n_k,n_q,n_r\}$ and $\{n_l,n_g,n_k,n_j\}$, respectively. Each element occupies a

hexahedral space. If the particle enters this space, it may collide with its corresponding element. For this process, the criterion is divided into two parts in sequence:

Part 1: Estimate whether the particle is in the range of the hexahedron occupied by the element in the y and the z directions. Taking Figure 8 as an example, the criterion is:

$$\text{If } \begin{cases} y_{\min} \le y_{p2} \le y_{\max} & y_p \in \underline{\mathbf{X}}(\mathbf{x}_{(p)}, t) \\ z_{\min} \le z_{p2} \le z_{\max} & z_p \in \underline{\mathbf{X}}(\mathbf{x}_{(p)}, t) \end{cases}, \text{ then } \mathbf{x}_{(p2)} \text{ is the candidate particle in contact with } e_{(2)}, \tag{14}$$

in which $y_{\min}$, $y_{\max}$, $z_{\min}$, and $z_{\max}$ are the minimum and maximum values of the four nodes of the elements $\mathbf{m}_{(nl)}$, $\mathbf{m}_{(ng)}$, $\mathbf{m}_{(nk)}$, and $\mathbf{m}_{(nj)}$ in the y and z directions, respectively.

Part 2: Estimate whether the particle is in the hexahedron occupied by the element. Taking Figure 8 as an example, A, B, C, and D are projections of n_l, n_g, n_k, and n_j in the x–y plane, respectively; p_2' is the projection of $\mathbf{x}_{(p2)}$. Then, the criterion is :

$$\text{If } \left| S_{ABCD} - (S_{ABp_{2'}} + S_{BCp_{2'}} + S_{CDp_{2'}} + S_{DAp_{2'}}) \right| \quad o \text{, then } \mathbf{x}_{(p2)} \text{ may contact } e_{(2)}, \tag{15}$$

where S represents the area of the triangle and o is an infinitesimal.

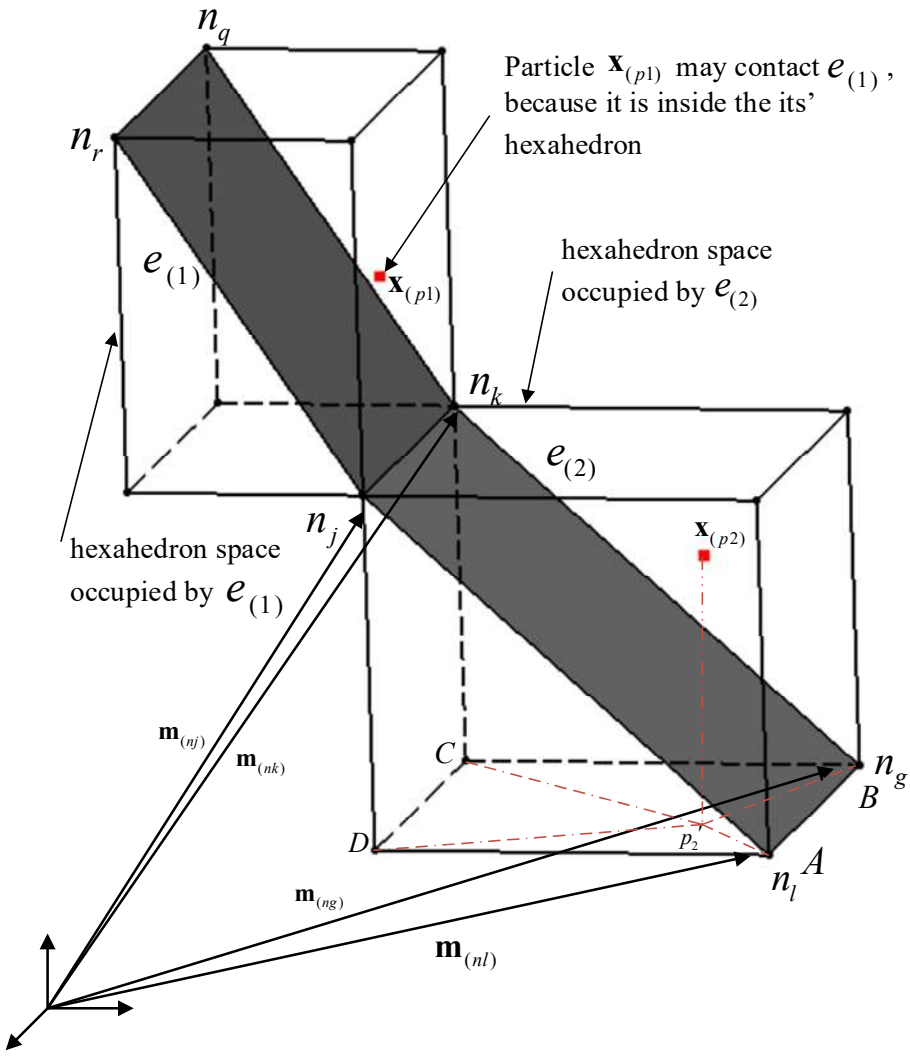

FIGURE 8 Schematic of particle–element contact detection

If the particle is located on one face or a corner of the hexahedron corresponding to the element, more than one and fewer than seven elements may collide with it.

3) Estimate whether particles penetrate elements. The relative positions of the point and the plane are analyzed based on their spatial geometry to this end. The equation of planar elements can be obtained through the coordinates of the elemental nodes, that is, $Ax+By+Cz+D=0$. Taking element $e_{(2)}$ as an example, the normal vector of the plane is calculated by:

$$\mathbf{n}_{e2} = (A, B, C) = (\mathbf{m}_{(nk)} - \mathbf{m}_{(nl)}) \times (\mathbf{m}_{(nj)} - \mathbf{m}_{(ng)}), \tag{16}$$

Then, D is calculated by $D = -(A * x_0 + B * y_0 + C * z_0)$, in which $M_0(x_0, y_0, z_0) \in e_{(2)}$. In step (1), the control nodes of the element are arranged in a clockwise or counterclockwise direction. Therefore, there are four situations to judge whether the particle has penetrated the impactor: Situation 1, normal vector points to the outside of the impactor and the particle has not penetrated the impactor; Situation 2, normal vector points to the outside of the impactor and the particle has penetrated the impactor; Situation 3, normal vector points to the inside of the impactor and the particle has not penetrated the impactor; Situation 4, normal vector points to the inside of the impactor and the particle has penetrated the impactor, as shown in Figure 3.9.

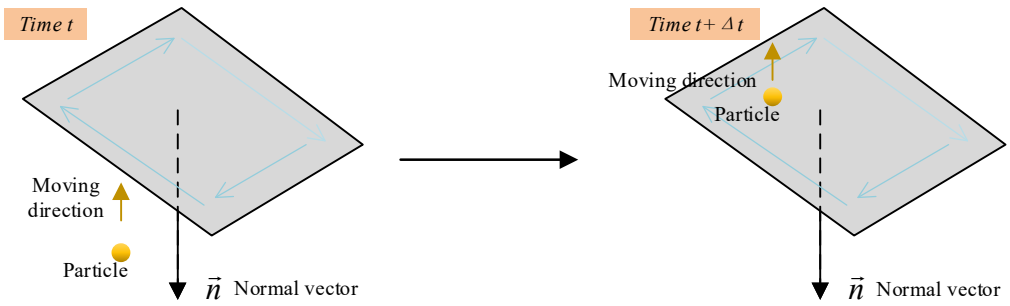

(a) Situation 1

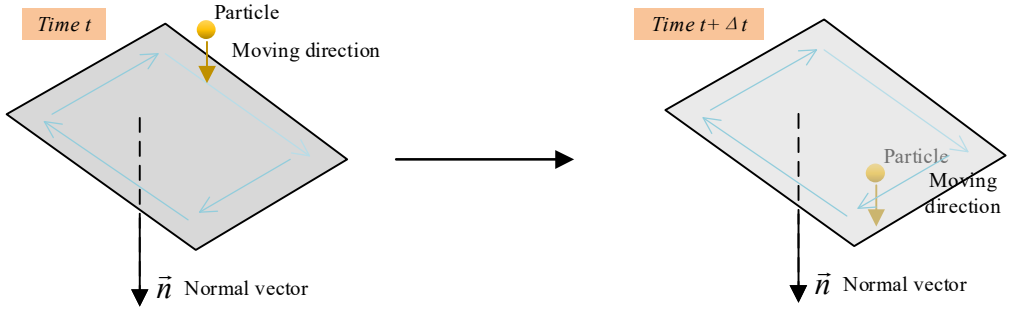

(b) Situation 2

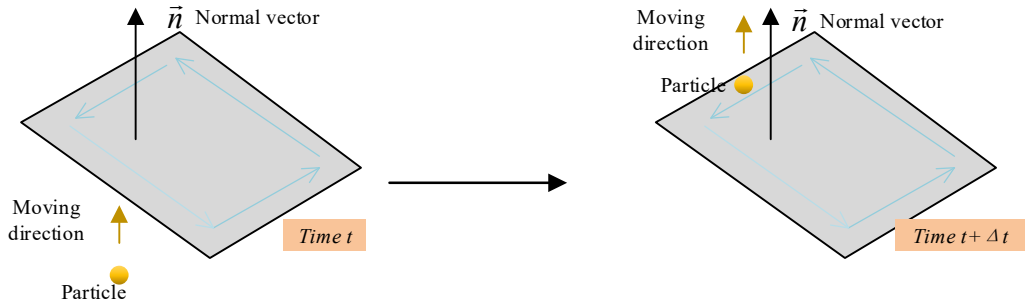

(c) Situation 3

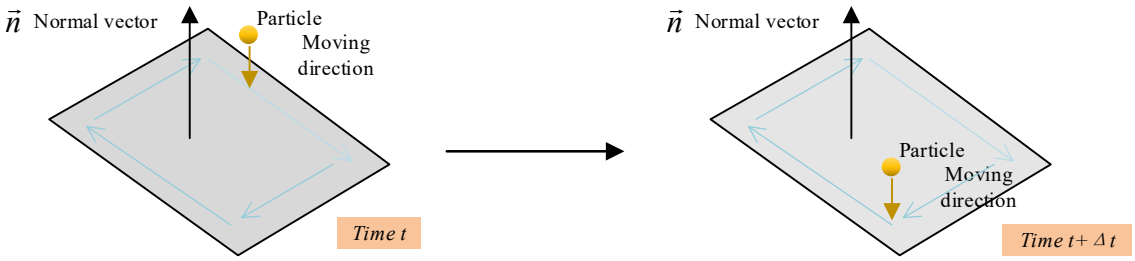

(d) Situation 4

FIGURE 9 Classification of positional relationship between the particle and the element

Then, the following simple criterion is developed to detect the penetrated particle and the element:

$$\text{If } \begin{cases} A*x_p^t + B*y_p^t + C*z_p^t + D \le 0 \;\&\; A*x_p^{t+\Delta t} + B*y_p^{t+\Delta t} + C*z_p^{t+\Delta t} + D > 0 \\ \text{or} \\ A*x_p^t + B*y_p^t + C*z_p^t + D \ge 0 \;\&\; A*x_p^{t+\Delta t} + B*y_p^{t+\Delta t} + C*z_p^{t+\Delta t} + D < 0 \end{cases} \text{ then contact occurs.} \tag{17}$$

Contact detection is thus completed. The relocation and the force of the particle in contact are calculated by following the procedure in Section 2.2, that is,

$$\bar{\mathbf{x}}_{(i)}^{t+\Delta t} = \mathbf{x}_{(pen)}^{t+\Delta t} + \bar{\mathbf{x}}_{(rel)}^{t+\Delta t} = \mathbf{x}_{(pen)}^{t+\Delta t} + d*\mathbf{n}, \tag{18}$$

with

$$d = \frac{Ax_p + By_p + Cz_p + D}{\sqrt{A^2 + B^2 + C^2}}. \tag{19}$$

4. Solution strategy for the FCCDA

The PD solver established here follows the recommendation in Chapter 7 of Ref. [11], and its framework is embedded into the PD solver as a subroutine. To better understand the strategy for contact detection in the PD solver, we first review its numerical solution of impact events. As shown in Figure 10, the contact detection procedure is an extra-iterative procedure embedded in the time integration part of the PD solver.

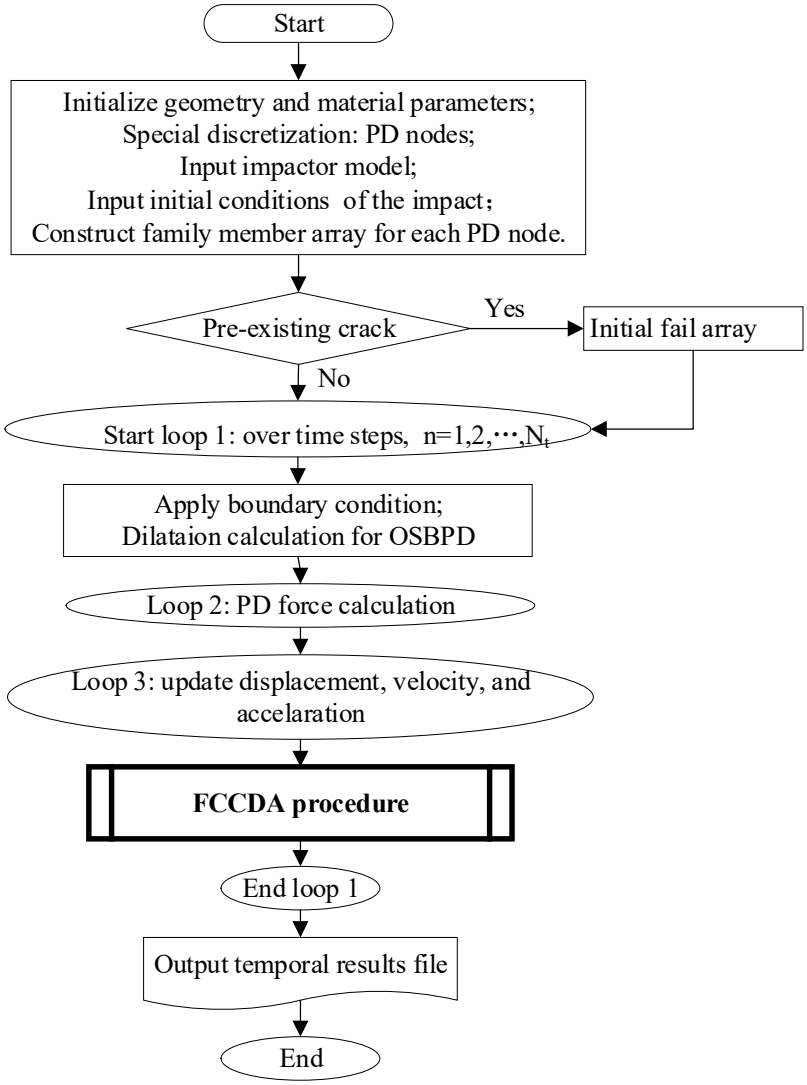

FIGURE 10 The framework of the FCCDA in the PD solver

Contact is detected and the contact force calculated in the FCCDA algorithm as shown in Figs.

11 and 12. Here, N_{node} represents the total number of material points in the PD domain, and N_e represents the total number of discretized elements of the impactor. A pointer parameter $P1$, whose value is zero in case of no contact and one in case of contact, is introduced to transfer the results of detection of the subroutines to the main program. Two subroutines make up the FCCDA framework; one is the main module controlling the start and end of contact detection, and to transfer relocation information to PD integration, as shown in Figure 11, and the other is an algorithm module to calculate the analytical geometry, shown in Figure 12.

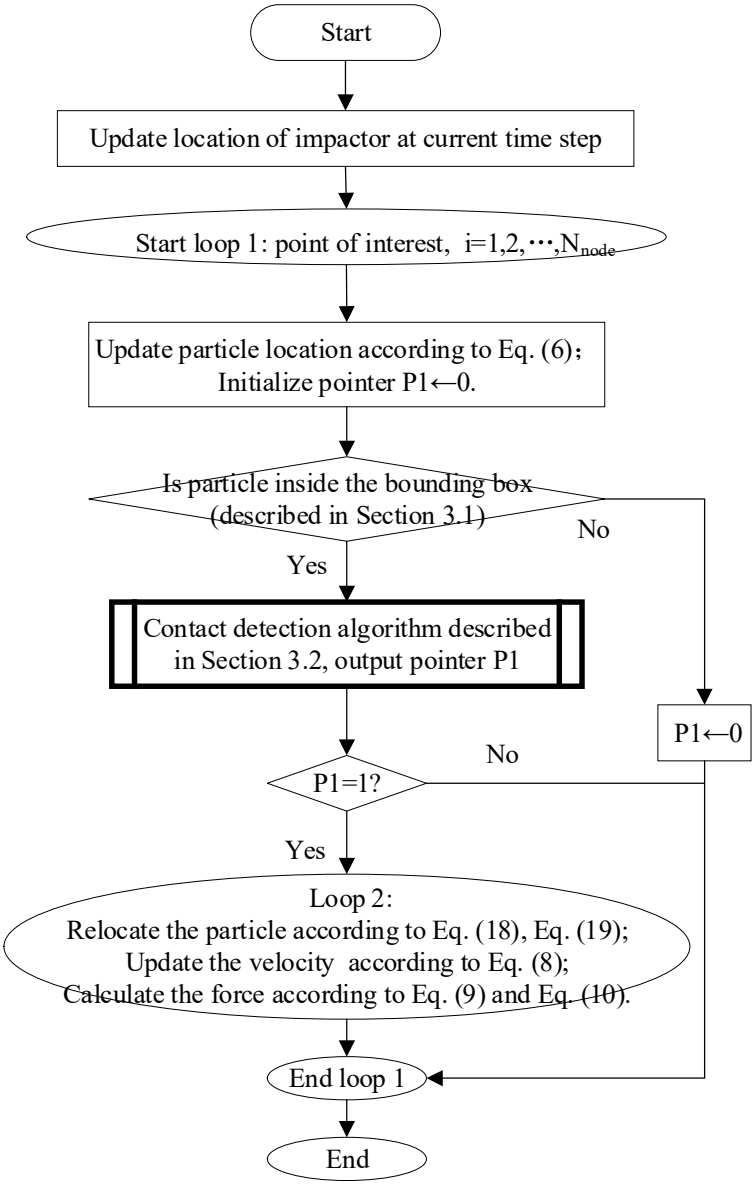

FIGURE 11 Flowchart of the algorithm for the FCCDA

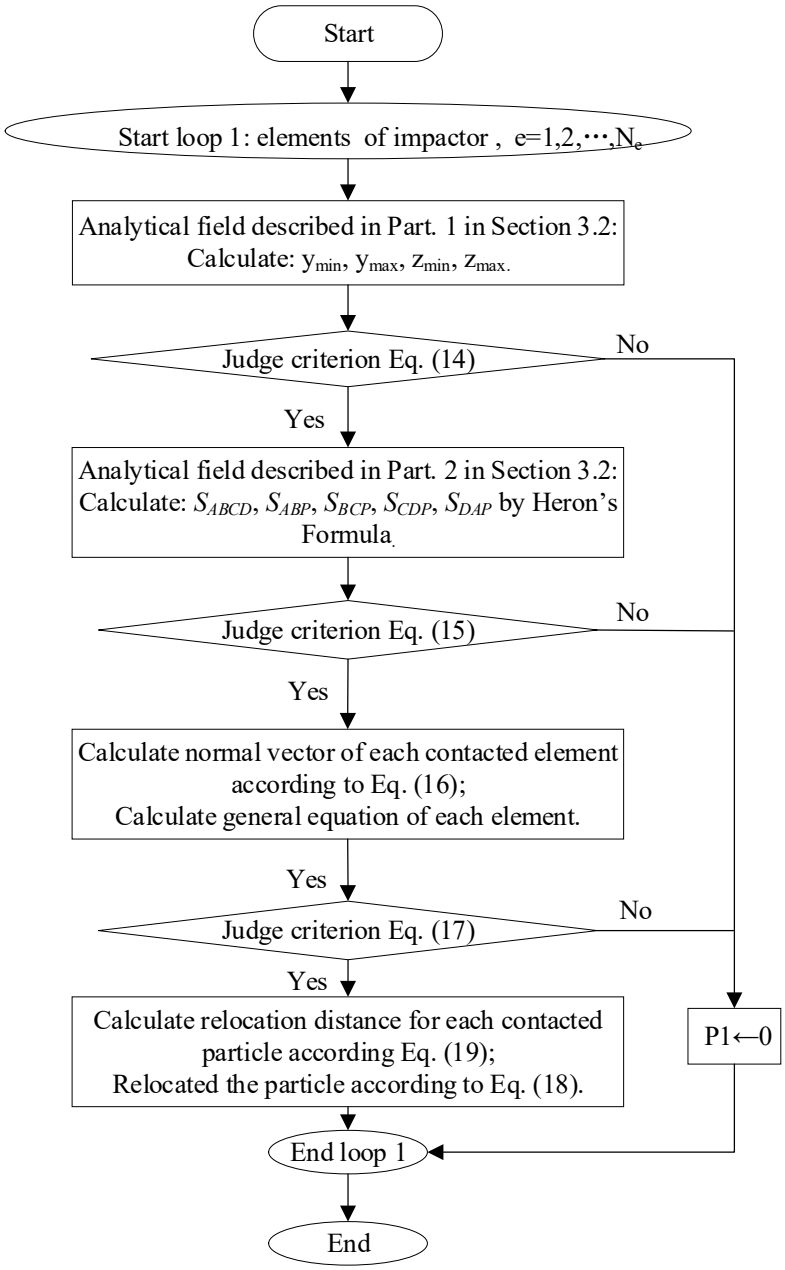

FIGURE 12 Flowchart of the contact detection algorithm presented in Figure 11

5. Validation on benchmark with a regular-shaped impactor

In this section, we examine the benchmark event of a rigid cylinder impacting a plate to validate the accuracy of the FCCDA and illustrate its implementation. The results were compared with those of the original PD and FEM calculations in Abaqus software, and were found to be in good agreement. Moreover, grid sensitivity analysis was conducted to examine the convergence and mesh size of the

proposed method.

5.1 Model setup

As shown in Figure 13, a rigid cylindrical wall impacted an isotropic elastic plate that was initially stationary without any constraint. The rigid cylinder had a diameter of D_C=0.05 m, thickness of H_C=0.025 m, and a mass of m_C=1.57 kg. It moved along the y direction with an initial velocity of v_C=32.0 m/s. The geometric dimensions of the plate were length L_p=0.2 m, width W_p=0.1 m, and thickness H_p=0.009 m. Its material properties were: elastic modulus E=191 GPa, Poisson's ratio υ=0.25, and mass density ρ=8000 kg/m^3. In the PD domain, the total number of material points in the x, y, and z directions were 200, 100, and nine, respectively. Furthermore, the spacing between particles was Δ_p=0.001 m, the time step for calculation was Δt=1.0×10^{-7} s, and the total number of time steps was t=2000.

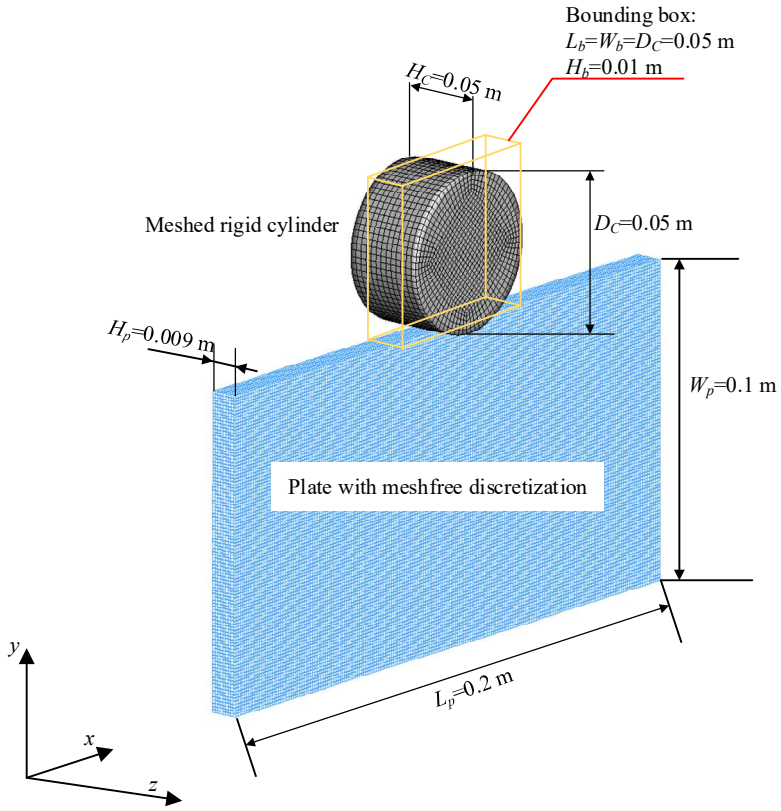

FIGURE 13 Model setup of a rigid cylinder impacting a rectangular plate

Note that the optimal scheme of the bounding box is for it to contain all possible contact meshes. It was established as a cuboid with geometric dimensions of L_b=W_b =D_C=0.05 m, and thickness H_b=0.01 m (slightly greater than the thickness of the plate). The bounding box moved with the impactor. This not only helped avoid searching for particles that could not collide with it, but also helped avoid searching for meshes that could not collide with the particles. This helped significantly reduce the amount of computation needed for contact detection. In addition, all mesh control nodes were arranged in counterclockwise order so that the normal vectors of the elements pointed to outside the cylinder. The criteria of contact detection for different parts of the cylinder are different according to Equation (17):

$$\begin{cases} A*x_p^t + B*y_p^t + C*z_p^t + D \le 0, \ \ if \ \ y_p^t \le p_c^t \\ \\ A*x_p^t + B*y_p^t + C*z_p^t + D \ge 0, \ \ if \ \ y_p^t > p_c^t \end{cases} \tag{20}$$

in which p_c^t represents the center of the cylinder at time step t.

5.2 Mesh sensitivity analysis and numerical results

The meshes of the cylindrical impactor were set to Δ_m=0.0001 m, Δ_m=0.0005 m, Δ_m=0.001 m, Δ_m=0.0015 m, and Δ_m=0.002 m, as shown in Figure 14. The particles in the picture are from the domain of PD discretization. Note that the mesh size Δ_m=0.0001 m is not depicted here owing to its poor clarity in a dense mesh.

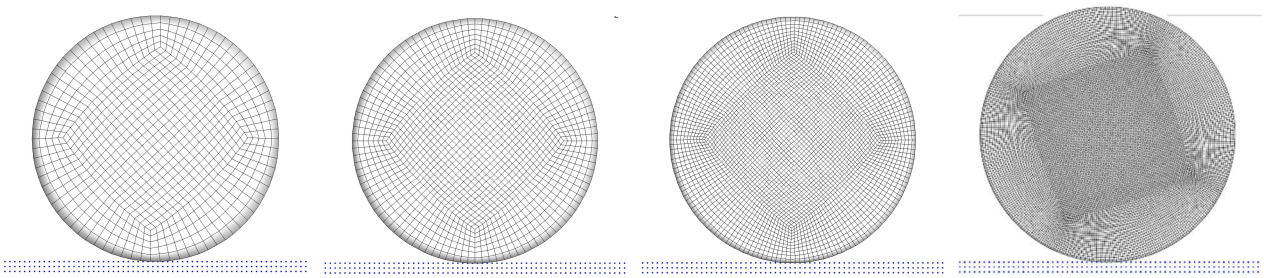

(a) Δ_m=0.002 m (b) Δ_m=0.0015 m (c) Δ_m=0.001 m (d) Δ_m=0.0005 m

FIGURE 14 Different mesh divisions

The results of calculation are provided in Figs. 15–17. Figure 15 shows the contours of the deformation of the plate in the x and y directions. The displacements in both directions were highly consistent. Because the impact-induced motion and deformation mainly occurred in the y direction, the deformation in the x direction was completely consistent. With the increase in grid size, a slight difference in deformation was obtained at the center of the plate. Consequently, under the condition that the mesh size was sufficiently large to encompass the outline of the impactor, it did not affect the convergence of the results of the FCCDA model, but was not very sensitive to the accuracy of the results. Therefore, we recommend examining the mesh size further to select an optimal grid size to ensure the accuracy and efficiency of the calculations.

Figs. 16 and 17 compare the curves of the PD solution with the results of the FEM (including the deformation of the plate in Figure 16 and the motion of the impactor in Figure 17). The results of the FEM were obtained using Abaqus, where the grid size of the plate was the same as the particle spacing in the PD domain, and that of the cylinder was identical to that in the PD scheme. The results show a remarkable agreement between the PD-FCCDA scheme and the results of the FEM, which demonstrates the validity of the former.

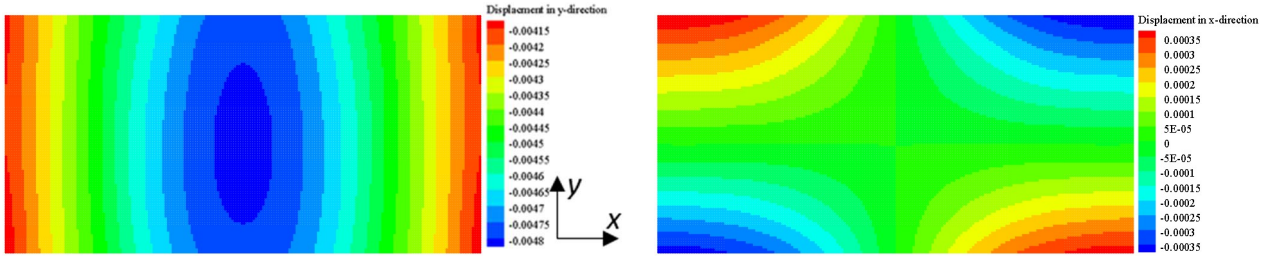

(a) Δ_m=0.002 m

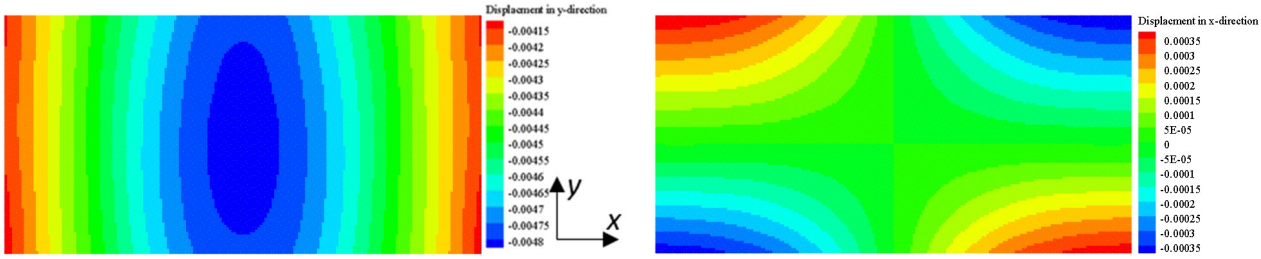

(b) Δ_m=0.0015 m

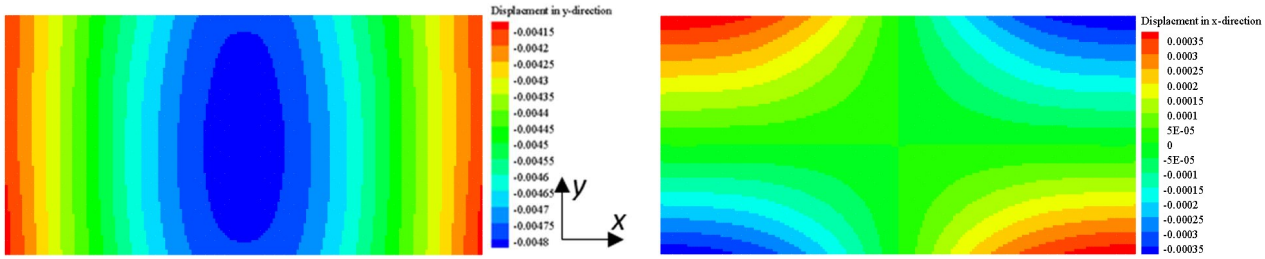

(c) Δ_m=0.001 m

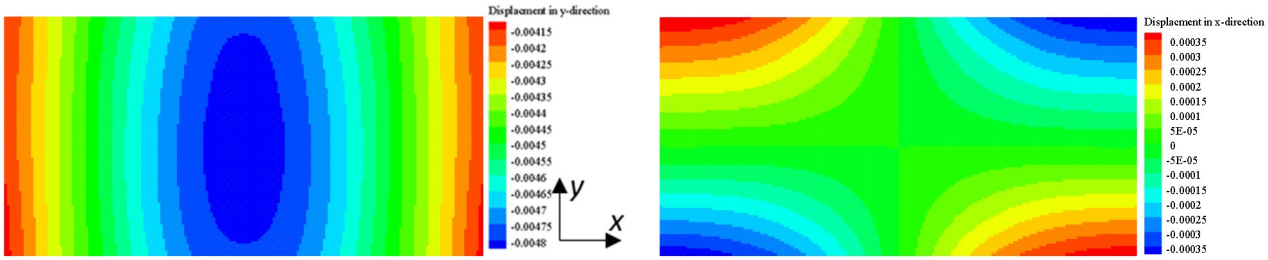

(d) Δ_m=0.0005 m

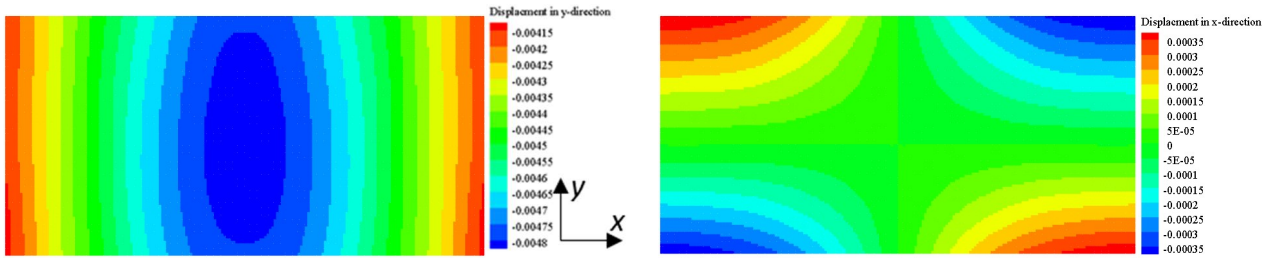

(e) Δ_m=0.0001 m

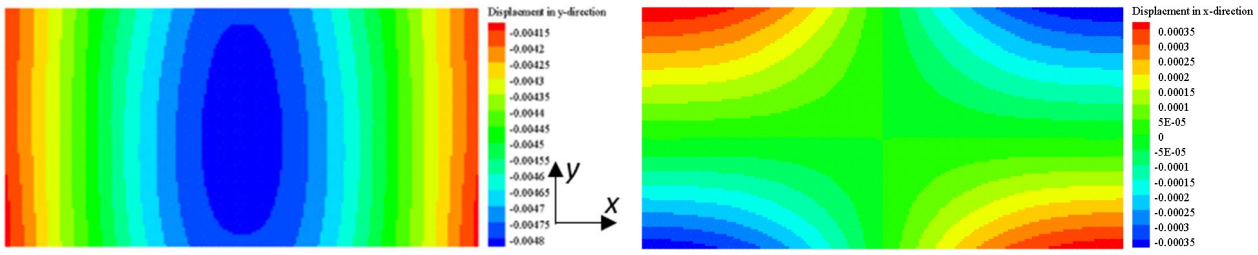

(f) original PD solution

FIGURE 15 Comparison of mesh sizes in the PD solution: displacements in the x (right) and y directions (left) of the plate when in contact with the cylinder. (color should be used)

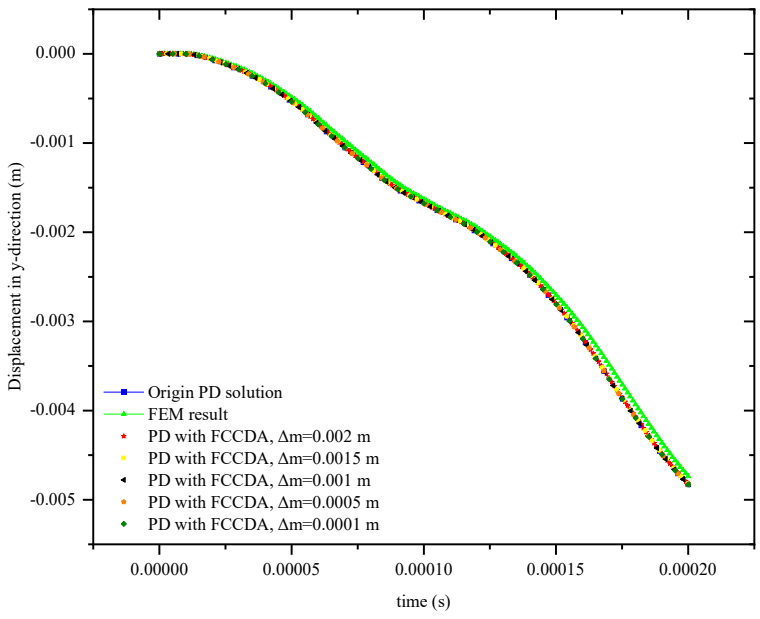

(a) PD and FEA predictions for the displacement component in the y-direction at the center of the plate as time progresses

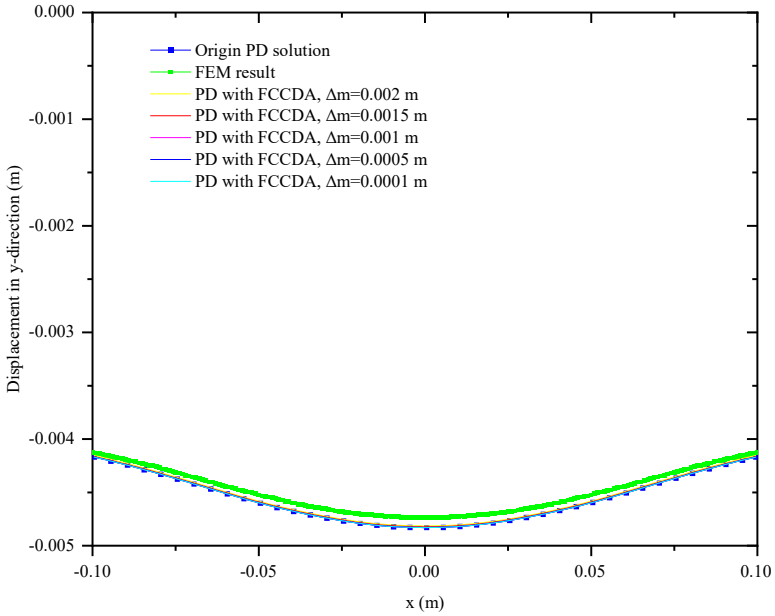

(b) PD and FEA displacement predictions in the y-direction at a time step of 2000 along the central x-axis

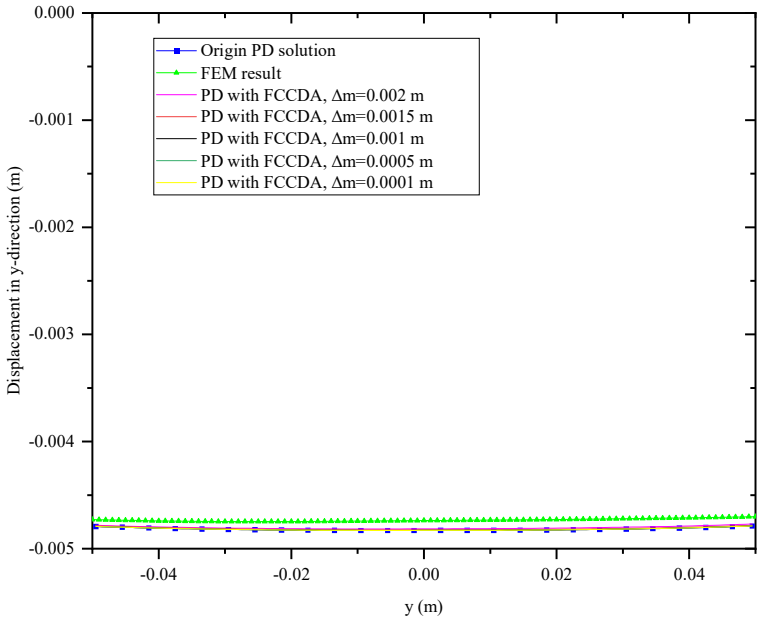

(c) PD and FEA displacement predictions in the y-direction at a time step of 2000 along the central y-axis

FIGURE 16 Comparison of the deformation of the plate in the PD solution and the FEM (color should be used)

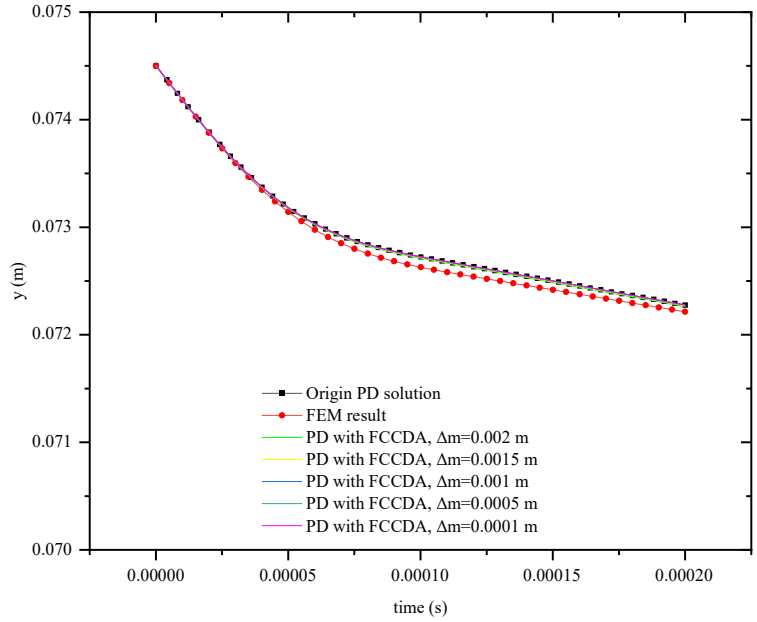

(a) PD and FEA predictions for the central position of the cylinder as time progresses

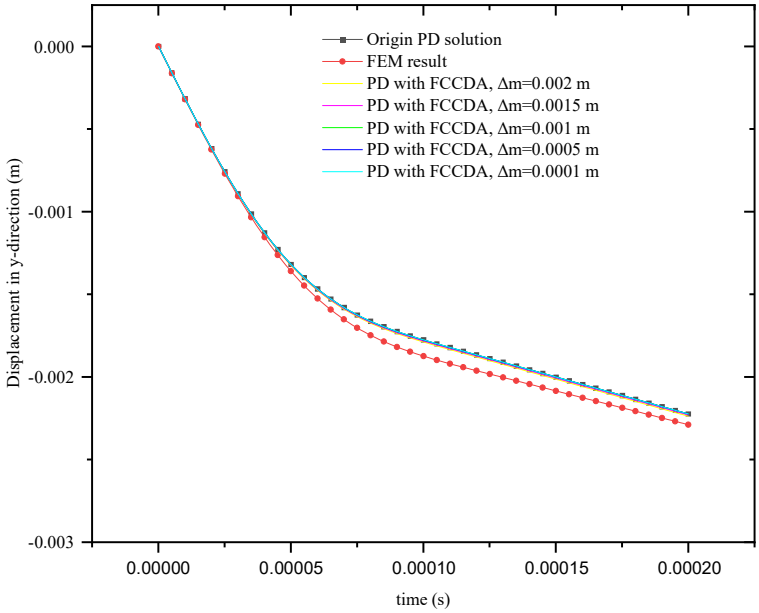

(b) PD and FEA predictions for the displacement component in the y-direction at the centre of the cylinder as time progresses

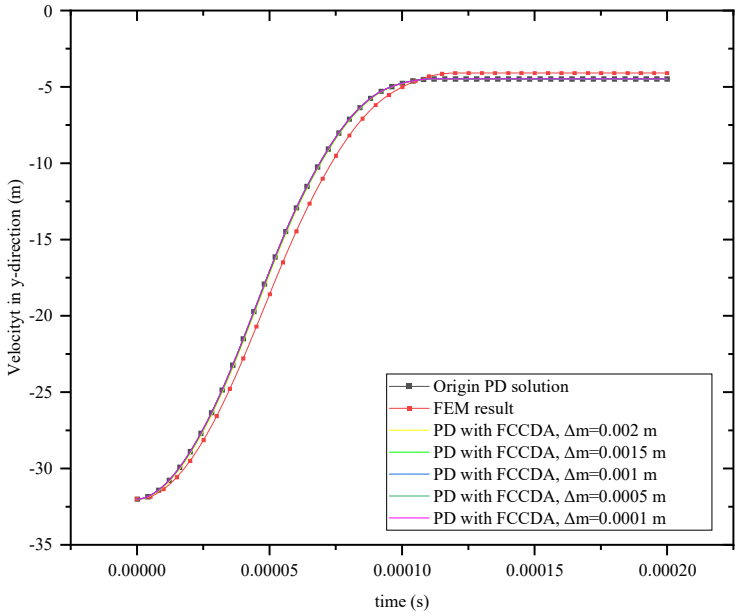

(c) PD and FEA predictions for the velocity component in the y-direction at the center of the cylinder as time progresses

FIGURE 17 Comparison of the movements of the impactor in the PD solution and the FEM (color should be used)

6. Engineering applications of irregular-shaped impactor

To show that the proposed algorithm is applicable to more complex conditions than those considered above, two engineering events are simulated in this section. The impactors in both cases were either irregular surfaces or complex surfaces with self-driven motion. The impactor considered in Section 6.1 was discretized by the preprocessor in LS DYNA while that in Section 6.2 was discretized by a meshing solver that we developed. The nodes of elements in both models were arranged in counterclockwise order.

6.1 A ship hull breaks through an ice sheet

The proposed algorithm was applied to interactions involving a ship and a submarine surfacing

through the ice in our previous work [15, 17, 28], in which numerical results had been compared with experimental results. In this section, we show the applicative value of the proposed algorithm and provide suggestions for tutorials for readers to apply the algorithm to their own cases. Note that the failure model in the PD method was included in the present case.

An icebreaker breaking level ice of uniform thickness was simulated. Its principal dimensions were: length on the waterline $L_{WL}=155\ m$, breadth $B_{WL}=23\ m$, draft $T=9\ m$, stem angle $\phi=24\ \deg$, and waterline angle $\alpha=22\ \deg$. The geometric dimensions of the ice plate were length $L_{ice}=150\ m$, width $B_{ice}=36\ m$, and thickness $H=2\ m$. The ice was assumed to be a homogeneous isotropic material with an elastic modulus of $E=1.8$ Gpa, Poisson's ratio $\nu=0.25$, and density $\rho=900\ kg/m^3$. The icebreaker broke ice at a speed of 3 knots. For the discretization of the information and the numerical simulation, the grid size was set to $\Delta x=L/240$ and the time step was $\Delta t=0.00376$ s.

Figure 18(a) gives the discretization of the impactor (ship model) and Figure 18(b) provides the bounding box of the ship model. The mesh of the bow of the ship was refined to precisely identify contact as most contact events occur in this area, and abrupt changes in the surface curvature of the ship are noticeable in the area of the bow. The bounding box had a regular hexahedral shape, and contained the entire hull. The height, length, and width of the hexahedron were equal to those of the hull, respectively.

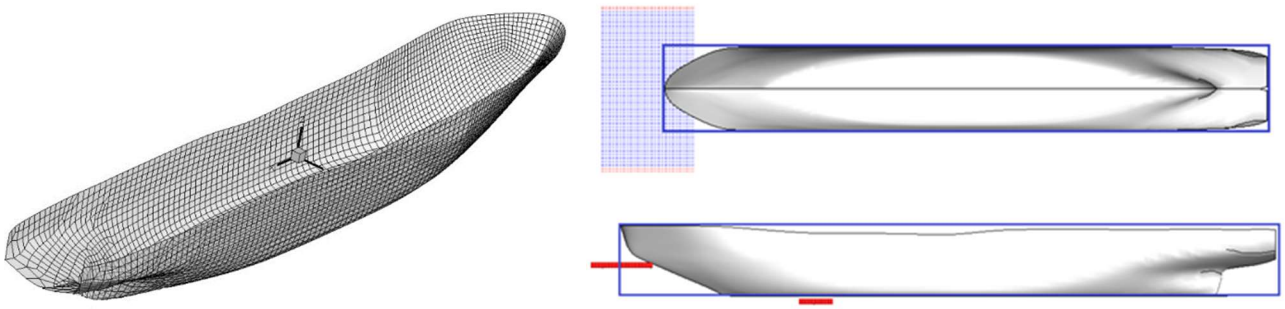

(a) the discretization of the impactor model (b) the model of boxing box

FIGURE 18 Scheme of the bounding box for the ship

Figure 19 shows the ice-breaking process at different times: The snapshots on the left are views of ice damage with the ship model while the images on the right show only ice damage corresponding to scenes on the left side. In each time step, the detection algorithm perfectly calculated and redistributed the PD particles that were in contact with the hull. The ice was broken around the surface of the hull according to the nature of its collision, and then moved away from the hull. The modes of failure and crack propagation of ice were remarkably consistent with empirical observations. The contact force in time was calculated by Equation (10) and is plotted in Figure 20. It shows that the contact force changed periodically over time. This explains the phenomenon whereby the detected particles of collision moved along the surface of the hull instead of impacting it when they were completely destroyed and redistributed to their new positions. This is consistent with ice–ship interactions. The force in the z direction was larger than that in the x direction because the inclined bow broke the ice plate through gravity. A majority of the particles in contact with it were redistributed vertically, which also demonstrate the efficiency of the FCCDA.

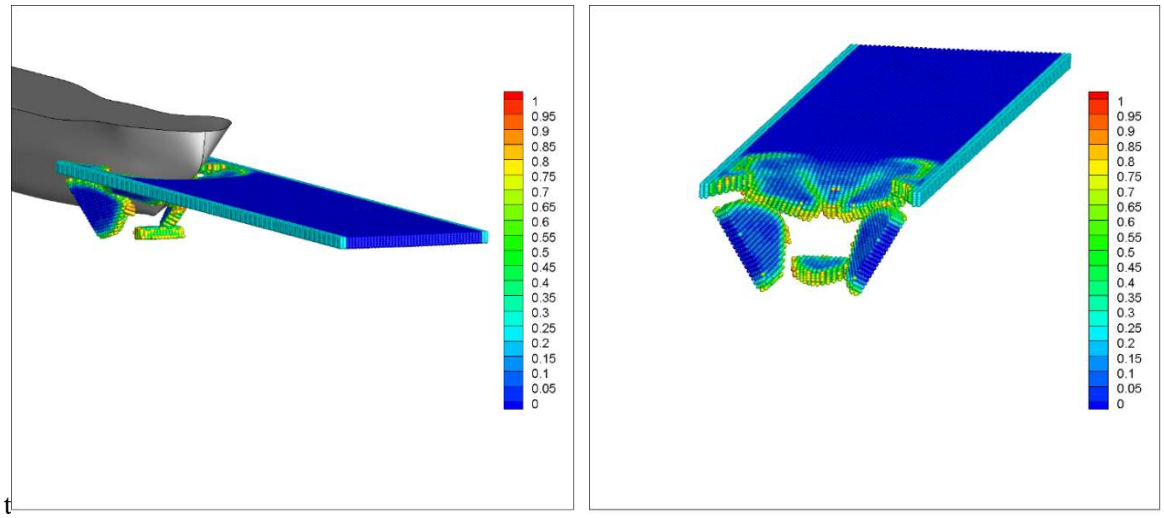

(a) $t = 18.8\ s$

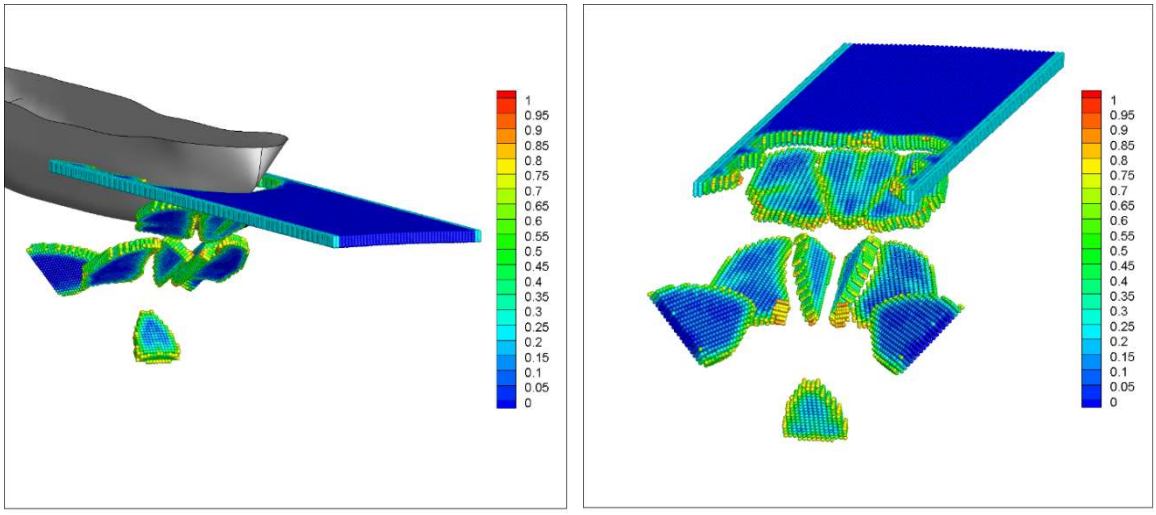

(b) $t = 37.6\ s$

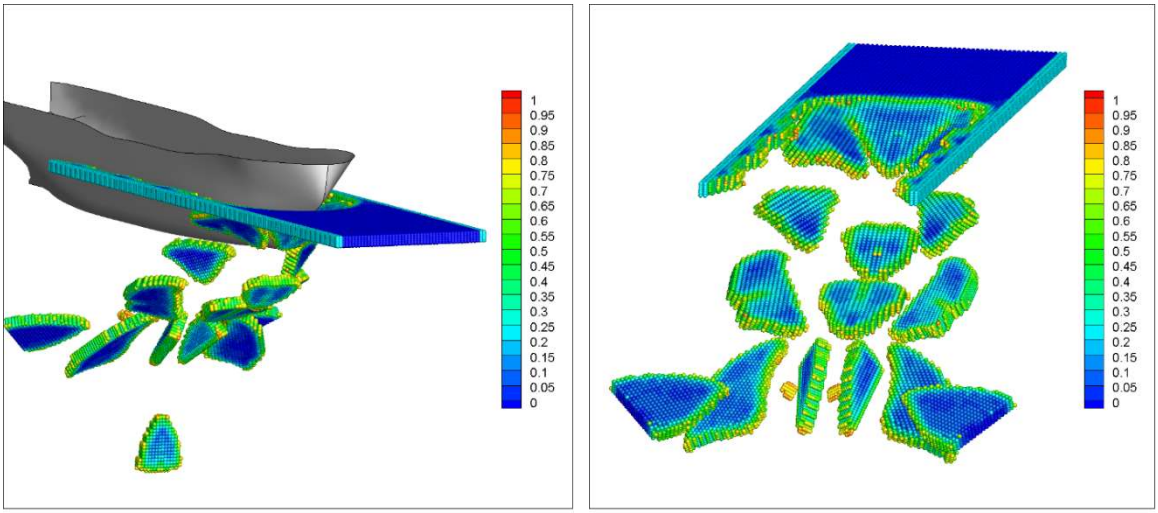

(c) $t = 56.4\ s$

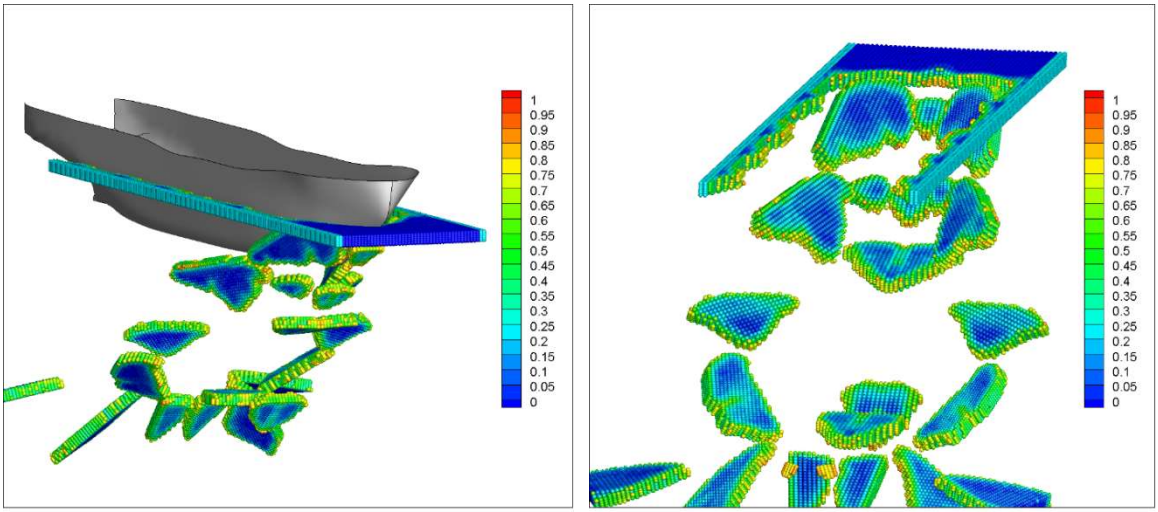

(c) $t = 75.2\ s$

FIGURE 19 Process of ship impacting ice

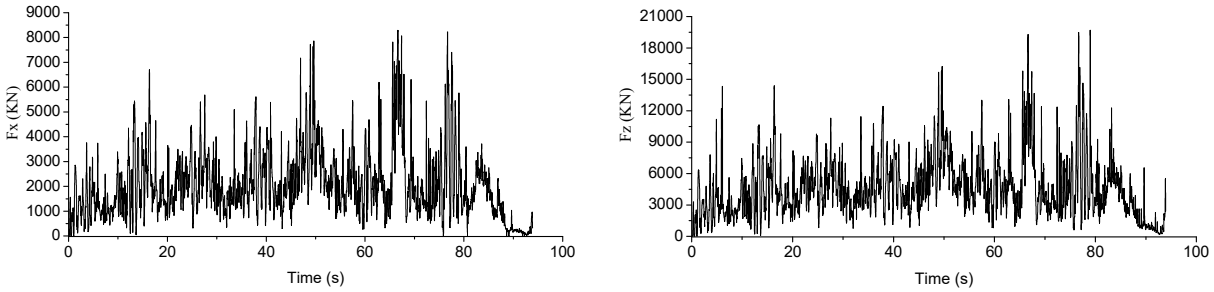

FIGURE 20 Curve of force of ship impacting ice

The above engineering case shows that the following should be addressed with regard to the numerical processing of different impact events when applying the proposed algorithm.

Grid refinement is an excellent method to improve the efficiency and accuracy of calculation, and is applicable to the following two situations: 1) In case of collision of a body with an irregular surface, appropriate mesh refinement measures can be used where the curvature changes significantly, while a coarse mesh can be used where the surface does not change significantly. 2) Different areas of the same impactor are in different degrees of contact with the target of collision, and thus the mesh can be refined in the critical area of the impactor.

6.2 A propeller in contact with an ice block

The geometry of the propeller is expressed by the chord length, pitch, thickness, camber, rake, and skew at different radii; it also rotates when operating. The outline of the propeller is much more complex than that of ships, and collision in it is accompanied by the rotation of its blades. This makes contact detection in case of collisions involving a propeller one of the more complex cases in engineering analysis. Ice–propeller interactions include cutting, collision, and milling. The application of the PD method and the contact detection algorithm to propeller–ice interaction during milling has been validated in our previous work [29, 30]. The purpose of considering such a case here

is to illustrate the efficient application of the proposed contact algorithm when encountering impact involving complex objects.

As shown in Figure 21(b), a propeller with four blades impacting an ice sphere was simulated. The propeller model was a product of the optimized design obtained by referring to the 1200 series R-class Ice Class propeller installed on the Canadian Coast Guard R-class icebreaker [31]. The parameters of the propeller model, as shown in Figure 20(a), were as follows: diameter $D_p = 4.12\ m$, hub-to-diameter ratio $r_h = 1.24$, and pitch ratio $P = 0.76$. The bounding box for propeller–ice contact was designed as depicted in Figure 6, and the details of the implementation of contact detection between the blades and ice have been provided in our previous work [29]. The mechanical properties of the ice sphere with a diameter $D = 0.01$ m were as follows: elastic modulus $E = 1.8$ GPa, Poisson's ratio $\upsilon = 0.25$, density $\rho = 900$ kg/m^3, critical stretch $s_0 = 0.032$, time step $\Delta t = 0.0348$ ms, and particle space $\Delta x = 0.0005$ m. The ice sphere moved with velocity $v_{ice} = 20.0$ m/s along the direction of the shaft of the propeller while the propeller rotated with a velocity of $v_{pro} = 3$ rps.

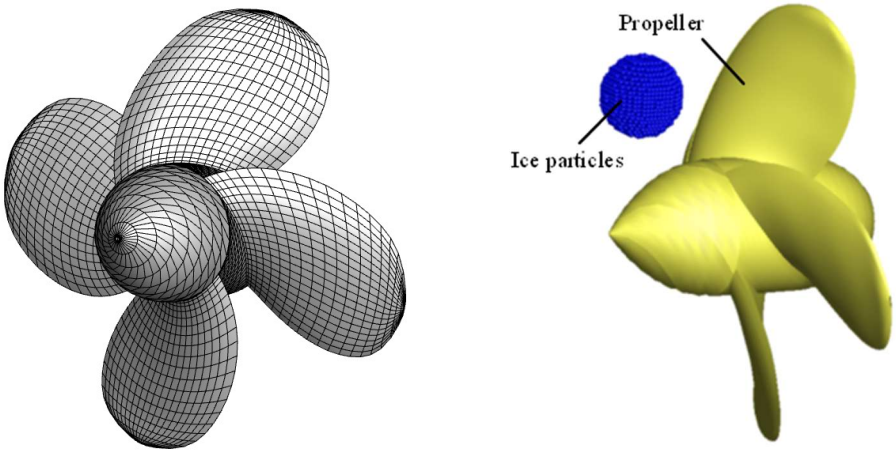

(a) The discretization of the propeller (b) ice-propeller contact model

FIGURE 21 Model of propeller impacting ice.

Figure 22 shows the ice breaking at different times when it collides with the propeller during the

reversal of the latter. When the ice hit the blades of the propeller, it broke into smaller pieces of varying sizes. The contact detection algorithm perfectly captured the ice particles in the collision area. The collision phenomenon also accorded with the empirical characteristics of collision in case of ice–propeller interaction.

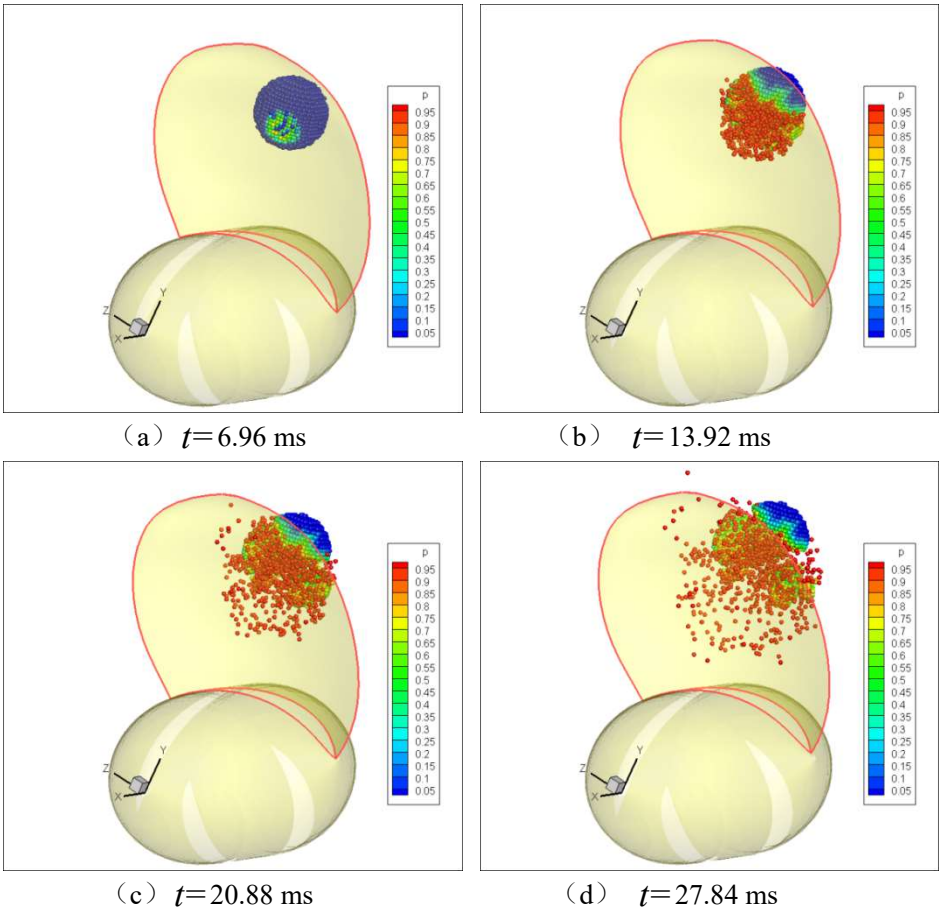

（a） t=6.96 ms　（b） t=13.92 ms

（c） t=20.88 ms　（d） t=27.84 ms

FIGURE 22 Dynamic process of ice failure in case of propeller–ice impact (reversal). (color should be used)

The above case shows that the FCCDA can be usefully applied to cases of the complex impact event, and can solve for contact related to unusual surface profiles and dynamic motion. It extends the scope of application of the PD method and generalizes the physical problems that it can solve.

7. Conclusions

This study proposes a fast and continuous contact detection algorithm (FCCDA) to detect contact in case of impact by using Peridynamics. The FCCDA discretizes the impactor into numbers of plane

elements, and detects contact by judging the positional relationship between the particles and planes in the PD domain based on geometric graphics. The algorithm consists of a bounding box and the process of contact detection. The bounding box reduces the need to search for unnecessary particles to make the method more efficient. The contact detection process is the core process of the algorithm, and involves the redistribution of particles in contact and the calculation of the contact force.

A benchmark case of a rigid cylinder impacting an elastic plate was used to validate the proposed model, and a sensitivity analysis of the mesh size was conducted to illustrate the characteristics of the proposed FCCDA. A good agreement was obtained between the results of the FEM and the PD solution. Moreover, two more engineering cases were used to highlight the advantages of its application to complex engineering problems.

The following conclusions can be drawn:

1) The benchmark cases showed that the proposed contact algorithm can accurately simulate the collision problem in PD mechanics.
2) The mesh size has a weak influence on the numerical results under the condition that the shape of the impactor is adequately modeled. However, a sensitivity analysis of mesh size is still recommended to ensure the accuracy of the method in specific cases.
3) The proposed algorithm has excellent applicative effect, and boasts advantages in solving collision problems involving objects with complex shapes.
4) For different impacting objects, mesh refinement can be carried out in case of sharp changes in shape or on key collision parts.

Although these have not been strictly derived and verified by numerical examination, the proposed method also has the following characteristics:

1) It can be applied to most particle-based methods, such as the SPH. These are non-local particle discretization methods like the PD method. Therefore, this method is applicable when calculating collision between SPH-controlled objects and arbitrary targets.

2) It can also be applied to the problem of coupling of particles and grid methods, such as the FEM, as it is based on the mesh-related features of surface form.

Acknowledgments

This research was supported by the National Natural Science Foundation of China (Grant No. 51809055), and the Natural Science Foundation of Heilongjiang Province of China (Grant No. E2018026).

References

[1] S. Oterkus. Peridynamics for the solution of multiphysics problems. The University of Arizona, 2015.

[2] C. Jakob, H. Konietzky. Particle Methods, An Overview Freiberg, 24 (2012). https://tu-freiberg.de/sites/default/files/media/professur-felsmechanik-32204/E-book/05_particle_methods.pdf.

[3] S. Li, W.K. Liu. Meshfree particle methods and their applications, Applied Mechanics Reviews, 55 (2002) 1-34. doi:10.1115/1.1431547.

[4] M. Isiet, I. Mišković, S. Mišković. Review of peridynamic modelling of material failure and damage due to impact, International Journal of Impact Engineering, 147 (2021). doi: 10.1016/j.ijimpeng.2020.103740.

[5] F. Bobaru, J.T. Foster, P.H. Geubelle, S.A. Silling. Handbook of Peridynamic Modeling, CRC Press, 2016. doi: 10.1201/9781315373331.

[6] M.H. Liu, Q. Wang, W. Lu. Peridynamic simulation of brittle-ice crushed by a vertical structure, International Journal of Naval Architecture and Ocean Engineering, 9 (2017) 209-218. doi: 10.1016/j.ijnaoe.2016.10.003.

[7] R.W. Liu, Y.Z. Xue, X.K. Lu, W.X. Cheng. Simulation of ship navigation in ice rubble based on peridynamics, Ocean Enging, 148 (2018) 286-298. doi: 10.1016/j.oceaneng.2017.11.034.

[8] C.T. Nguyen, S. Oterkus. Peridynamics for the thermomechanical behavior of shell structures, Engineering Fracture Mechanics, 219 (2019). doi: 10.1016/j.engfracmech.2019.106623.

[9] E.G. Nezami, Y.M.A. Hashash, D.W. Zhao, J. Ghaboussi. A fast contact detection algorithm for 3-D discrete element method, Computers and Geotechnics, 31 (2004) 575-587. doi: 10.1016/j.compgeo.2004.08.002.

[10] S.A. Silling, E. Askari. Peridynamic modeling of impact damage, in: ASME/JSME 2004 pressure vessels and piping conference, American Society of Mechanical Engineers, 2004, pp. 197-205. doi: 10.1115/PVP2004-3049.

[11] E. Madenci, E. Oterkus. Peridynamic Theory and Its Applications (2014). doi: 10.1007/978-1-4614-8465-3.

[12] B. Vazic, E. Oterkus, S. Oterkus. Peridynamic approach for modelling ice-structure interactions, in: Trends in the Analysis and Design of Marine Structures: Proceedings of the 7th International Conference on Marine Structures CRC Press, Dubrovnik, Croatia, 2019. doi: 10.1201/9780429298875-6.

[13] Y. Song, H. Yu, Z. Kang. Numerical study on ice fragmentation by impact based on non-ordinary state-based peridynamics, Journal of

Micromechanics and Molecular Physics, 04 (2019) 1850006. doi: 10.1142/s2424913018500066.

[14] B. Vazic. Multi-scale modelling of ice-structure interactions. University of Strathclyde, (2020).

[15] Y. Zhang, L. Tao, C. Wang, L. Ye, S. Sun. Numerical study of icebreaking process with two different bow shapes based on developed particle method in parallel scheme, Applied Ocean Research, 114 (2021) 102777. doi: 10.1016/j.apor.2021.102777.

[16] A. Javili, R. Morasata, E. Oterkus, S. Oterkus. Peridynamics review, Mathematics and Mechanics of Solids, 24 (2019) 3714-3739. doi: 10.1177/1081286518803411.

[17] Z. Yuan, T. Longbin, W. Chao, Y. Liyu, G. Chunyu. Numerical study on dynamic icebreaking process of an icebreaker by ordinary state-based peridynamics and continuous contact detection algorithm, Ocean Enging, 233 (2021) 109148. doi: 10.1016/J.OCEANENG.2021.109148.

[18] Y. Zhang, C. Wang, C. Guo, L. Tao. Peridynamic Analysis of Fragmentation of Ice Plate Under Explosive Loading With Thermal Effects, in: ASME 2020 39th International Conference on Ocean, Offshore and Arctic Engineering, 2020. doi: 10.1115/OMAE2020-18731.

[19] G. Hattori, M. Hobbs, J. Orr. A Review on the Developments of Peridynamics for Reinforced Concrete Structures, Archives of Computational Methods in Engineering, (2021). doi: 10.1007/s11831-021-09549-y.

[20] X.-P. Zhou, Y.-T. Wang. State-of-the-Art Review on the Progressive Failure Characteristics of Geomaterials in Peridynamic Theory, Journal of Engineering Mechanics, 147 (2021) 03120001. doi: 10.1061/(asce)em.1943-7889.0001876.

[21] P. Diehl, R. Lipton, T. Wick, M. Tyagi. A comparative review of peridynamics and phase-field models for engineering fracture mechanics, (2021). doi: 10.31224/osf.io/gty2b.

[22] S.A. Silling. EMU user's manual, Code Ver. 2.6d, National Laboratories, Albuquerque, (2004).

[23] J.G. Malone, N.L. Johnson. A parallel finite element contact/impact algorithm for non-linear explicit transient analysis: Part I—The search algorithm and contact mechanics, International Journal for Numerical Methods in Engineering, 37 (1994) 559-590. doi: 10.1002/nme.1620370403.

[24] J.G. Malone, N.L. Johnson. A parallel finite element contact/impact algorithm for non-linear explicit transient analysis: Part II—Parallel implementation, International Journal for Numerical Methods in Engineering, 37 (1994) 591-603. doi: 10.1002/nme.1620370404.

[25] P. Huang, Y. Ding, Q. Miao, G. Sang, M. Jia. An improved contact detection algorithm for bonded particles based on multi-level grid and bounding box in DEM simulation, Powder Technology, 374 (2020) 577-596. doi: 10.1016/j.powtec.2020.07.022.

[26] L.E. Walizer, J.F. Peters. A bounding box search algorithm for DEM simulation, Computer Physics Communications, 182 (2011) 281-288. doi: 10.1016/j.cpc.2010.09.008.

[27] S.W. Attaway, B.A. Hendrickson, S.J. Plimpton, et al. A parallel contact detection algorithm for transient solid dynamics simulations using PRONTO3D, Computational Mechanics, 22 (1998) 143-159. doi: 10.1007/s004660050348.

[28] L.Y. Ye, C.Y. Guo, C. Wang, C.H. Wang, X. Chang. Peridynamic solution for submarine surfacing through ice, Ships and Offshore Structures, 15 (2020) 535-549. doi: 10.1080/17445302.2019.1661626.

[29] L.Y. Ye, C. Wang, X. Chang, H.Y. Zhang. Propeller-ice contact modeling with peridynamics, Ocean Enging, 139 (2017) 54-64. doi: 10.1016/j.oceaneng.2017.04.037.

[30] C. Wang, W.P. Xiong, X. Chang, L.Y. Ye, X. Li. Analysis of variable working conditions for propeller-ice interaction, Ocean Enging, 156 (2018) 277-293. doi: 10.1016/j.oceaneng.2018.02.026.

[31] D.L.N. Walker. The influence of blockage and cavitation on the hydrodynamic performance of ice class propellers in blocked flow. Memorial University of Newfoundland, 1996.